Huang *et al. Cell Communication and Signaling* (2025) 23:124
https://doi.org/10.1186/s12964-025-02125-y

Cell Communication and Signaling

RESEARCH Open Access

Extracellular vesicular delivery of ceramides from pulmonary macrophages to endothelial cells facilitates chronic obstructive pulmonary disease

Qiqing Huang[1], Tutu Kang[1], Shaoran Shen[1], Lele Liu[1], Lili Zhang[1], Xiaoli Zou[1] and Jianqing Wu[1*]

Abstract

Background Ceramides are known for their harmful, cell-autonomous effects in cigarette smoke (CS)-triggered chronic obstructive pulmonary disease (COPD), yet their potential role as intercellular signals in COPD pathogenesis remains unclear. This study aims to investigate whether ceramides act as cell-nonautonomous mediators of COPD development by transmitting metabolic stress from pulmonary macrophages to endothelial cells (ECs), compromising endothelial function and thereby orchestrating the pulmonary inflammation.

Methods We analyzed single-cell RNA sequencing data from human lung tissues and bulk RNA sequencing data from alveolar macrophages (AMs) in COPD patients to investigate the transcriptomic profiles of ceramide biosynthesis enzymes. The expression changes of several key enzymes were validated in human lung sections, AMs isolated from CS-exposed mice, and cigarette smoke extract (CSE)-treated macrophages. Ceramide levels in macrophages and their extracellular vesicles (EVs) were quantified using mass spectroscopy lipidomics. EVs were further characterized by transmission electron microscopy and nanoparticle tracking analysis. The uptake of macrophage-derived EVs by ECs and their effects on endothelial barriers were evaluated in vitro using a co-culture system and in vivo using a CS-exposed COPD mouse model.

Results CS exposure upregulated enzymes involved in de novo ceramide biosynthesis in pulmonary macrophages, increasing levels of long- and very long-chain ceramides. These ceramides were packaged into EVs and delivered to ECs, where they disrupted gap junctions, increased endothelial permeability, and impaired EC migration. Silencing these enzymes involved in de novo ceramide biosynthesis in pulmonary macrophages could block this metabolic communication between macrophages and ECs mediated by EV-delivered ceramides, protecting EC function from CS exposure. When intratracheally administered to CS-exposed mice, these ceramide-rich macrophage-derived EVs exacerbated COPD by facilitating endothelial barrier disruption.

*Correspondence:
Jianqing Wu
jwuny@njmu.edu.cn

Full list of author information is available at the end of the article

Conclusion Our study uncovered a novel mechanism in COPD pathogenesis, where pulmonary macrophages propagate CS-induced metabolic stress to ECs via ceramide-laden EVs, leading to endothelial barrier dysfunction. This intercellular pathway represents a potential target for therapeutic intervention in COPD.

Plain English summary

Chronic obstructive pulmonary disease (COPD) is a condition caused by damage to the airways or other parts of the lung and is often triggered by smoking. This damage triggers inflammation and other changes that block airflow and make breathing difficult. While we know that ceramides, a type of fat molecule, can harm cells inside the lungs, it was unclear how they might affect different cells in the body. In this study, we explored how ceramides move between cells and how they might contribute to COPD. We found that cigarette smoke increases ceramide production in a type of lung immune cells called macrophages. These ceramides are then packaged into tiny particles called extracellular vesicles and released from macrophages, which travel to other cells, especially cells lining the blood vessels (endothelial cells). Upon entering endothelial cells, these ceramides disrupt the function of endothelial cells, making the lung's blood vessels more leaky and damaging their ability to repair. This process worsens the condition of COPD. Our study suggests that ceramides could be a new target for treating COPD by blocking this harmful communication between cells.

Graphical Abstract

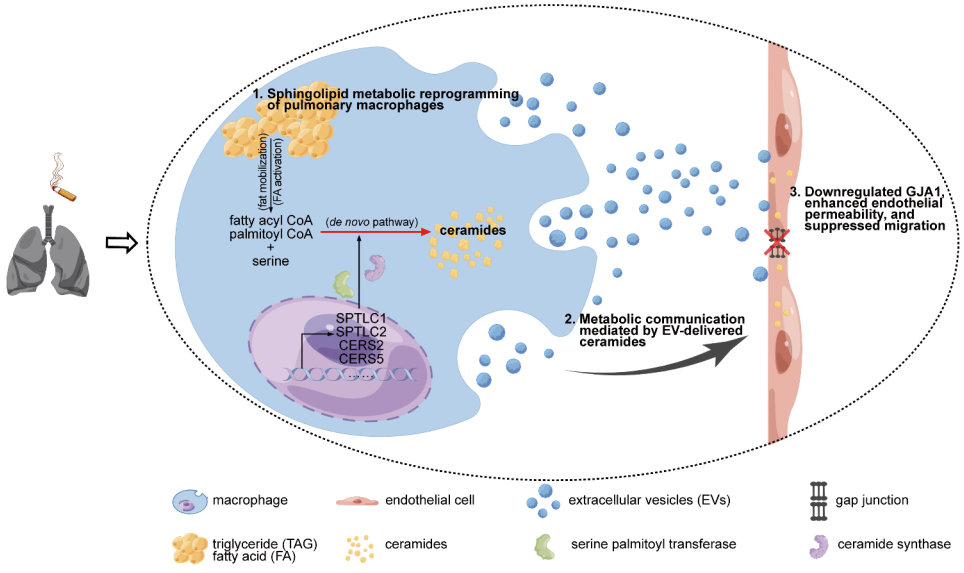

Keywords COPD, Macrophages, Endothelial cells, Ceramide, Extracellular vesicles, Immunometabolism

Background

Sphingolipids are a distinct class of lipids, primarily located in plasma membranes, with ceramides serving as a central hub in sphingolipid metabolism. Composed of a sphingosine backbone and a fatty acid side chain, ceramides are classified by the length of their N-acyl chains into medium-chain (C12-C14), long-chain (C16-C18), very long-chain (C20-C24), and ultra-long-chain (≥ C26) ceramides [1]. There are three major pathways responsible for ceramide biosynthesis, each regulated by specific enzymes: (1) the de novo synthesis pathway, starting with the condensation of serine and palmitoyl-CoA; (2) the sphingomyelinase pathway, which involves the hydrolysis of sphingomyelin; and (3) the salvage/recycling pathway, which regenerates ceramides from the breakdown of complex sphingolipids [2]. In addition to forming part of the plasma membrane, ceramides, sphingosine, and their metabolites—ceramide-1-phosphate (C1P) and sphingosine-1-phosphate (S1P)—constitute a "sphingolipid rheostat" [3], regulating various biological processes such as cell death, proliferation, differentiation, autophagy, senescence, migration, and efferocytosis [2]. Ceramides are also transported extracellularly via extracellular vesicles (EVs), which grants them a role as transcellular signals, facilitating metabolic communication between cells. This capacity for intercellular communication suggests that ceramides may contribute to disease development beyond their cell-autonomous effects [4, 5].

Cigarette smoking, the leading cause of chronic obstructive pulmonary disease (COPD), has been linked

to sphingolipid metabolic reprogramming in both plasma [6] and lung tissue [7] from COPD patients. Elevated ceramides have been implicated in cigarette smoke (CS)-induced injury of pulmonary endothelial and alveolar epithelial cells [8, 9], as well as the impairment of alveolar macrophage (AM) efferocytosis [10]. Although the intracellular effects of increased ceramides, particularly in cell-autonomous lung damage and macrophage dysfunction, have been well-established, the intercellular role of ceramides as part of an extracellular signaling machinery via EVs remains poorly understood in the context of COPD.

Recent transcriptomic studies of AMs from COPD patients and smokers have identified lipid metabolic dysregulation as a key driver of pulmonary pathology [11–14]. Our previous single-cell RNA-sequencing (scRNA-seq) of lung tissues from control and COPD patients with different smoking histories identified macrophages as the cells most affected by CS, with genes related to sphingolipid biosynthesis, vesicle-mediated transport, membrane organization, and mitochondrial gene expression being significantly altered [15]. Importantly, our in silico analysis further indicated that macrophage-derived sphingolipid metabolites, potentially transported via EVs, may influence endothelial cell (EC) gap junctions and migration, especially in the context of smoking [15].

Given the established role of endothelial barrier dysfunction in the pathogenesis of COPD and emphysema [16–19] and inspired by our prior findings [15], here we further investigate the EV-dependent mechanism through which CS-induced macrophage sphingolipid metabolic reprogramming leads to endothelial barrier disruption and ultimately contributes to COPD progression.

Methods

Ethics statement

This study was approved by the Ethics Committee at the First Affiliated Hospital of Nanjing Medical University (2021-SR-335). All animal experiments were approved by the Institutional Animal Care and Use Committee at Nanjing Medical University, carried out in accordance with the U.K. Animals (Scientific Procedures) Act, 1986 and associated guidelines as well as EU Directive 2010/63/EU for animal experiments, and complied with the ARRIVE guidelines.

Data resource and analysis

Single cell RNA transcriptomics of 3 COPD patients (2 smokers and 1 non-smoker) and 6 controls (2 smokers and 4 non-smokers) were from our previous dataset GSE171541 [15]. The BD Rhapsody analysis pipeline was used to process sequencing data and the reference genome was GENCODE v29. Expression matrix was processed with the Seurat (version 3·1·5). The cells were removed that had either fewer than 300 expressed genes or over 30% unique molecular identifiers (UMIs) originating from mitochondrial genes. UMI counts were normalized and were transformed to the log-transformed. Visualization of transcriptomic profiles were conducted by uniform manifold approximation and projection (UMAP). We used the AddModuleScore() function in Seurat to calculate a module score for the gene set *SPTLC1*, *SPTLC2*, *CERS2*, and *CERS5*, reflecting their average expression relative to a background set of control genes. Reanalysis was carried out of scRNA-seq datasets of human lung tissues (GSE173896, EGAS00001004244) as well as bulk RNA-seq datasets (GSE13896, GSE130928, and GSE183983) of AMs from smokers and COPD patients downloaded from Gene Expression Omnibus (GEO) (http://www.ncbi.nlm.nih.gov/geo/) and European Genome-phenome Archive (EGA) (https://ega-archive.org). RNA-seq data of mouse lung ECs after one and six months of exposure to whole body smoke compared to controls at room air (GSE140413) was obtained from GEO.

Mice and CS exposure

Male C57BL/6J mice of 8 weeks were purchased from the National Resource Center for Mutant Mice Model Animal Research Center of Nanjing University. Mice were randomly selected and exposed to cigarette smoke (CS) or room air (Air) for 6 months. CS exposures were performed via the CSM-100 C inhalation exposure apparatus (TOW-int tech, Shanghai, China) using Huangshan Brand cigarettes (China Tobacco Anhui Industrial Co., Ltd, Bengbu, Anhui, China). During CS exposure, total particulate matter (TPM) was real-time monitored by Microdust Pro Real Time Dust Monitor (Casella, Germay). Mice were exposed to an average TPM of 500 mg/m^3 and carbon monoxide (CO) concentration of 300 parts per million (ppm) for 1 h at a time, twice per day, 7 days a week for 6 months. Finally, mouse lung tissues were harvested for histopathological analysis to confirm the successful construction of CS-induced COPD mouse model.

Isolation and identification of primary mouse AMs

At the end of the exposure regimen, primary mouse AMs were isolated from bronchoalveolar lavage fluids (BALFs) as described previously [20]. Briefly, mice were anaesthetized with avertin (Sigma Aldrich, Cat# T48402). After the mouse trachea was opened and cannulated with a 26 G syringe needle (BD, Franklin Lakes, NJ, USA), the lung was lavaged with a total of 15 ml ice-cold PBS in 20 aliquots (0.75 ml per aliquot). The BALFs of every mouse were centrifuged at 300 g, 4 °C for 15 min. Cell pellets

were resuspended and cultured in RPMI 1640 (ThermoFisher, Gibco, Cat# 11875093) with 100 μg/ml streptomycin, 100 U/ml penicillin, 10 mmol/l HEPES (Sigma Aldrich, Cat# H4034), and 50 μmol/l β-mercaptoethanol (Sigma Aldrich, Cat# M3148) at 37 °C in a humidified 5% CO_2 atmosphere. After 1 h, other suspended blood cells were washed off by sterile PBS and the left adherent cells were pure primary mouse AMs. Mouse AMs were identified by flow cytometric analysis of mouse macrophage surface marker, F4/80. Briefly, AMs were collected and resuspended to a concentration of 1×10^6 cells/ml in 1% bovine serum albumin (BSA, dissolved in PBS) (Sigma Aldrich, Cat# A1933). Then, 0.1 ml of cell suspension was mixed and incubated with rat anti-F4/80 (1:50, Abcam, Cambridge, UK, Cat# ab6640) or anti-rat IgG (1:50, Abcam, Cat# ab37361) at room temperature for 30 min. After being washed by 1% BSA, cells were resuspended in 0.1 ml of 1% BSA and incubated in dark with anti-rat IgG Alexa Fluor 488 (1:2000, Abcam, Cat# ab150165) at room temperature for 30 min. The stained cells were washed twice with 1% BSA and were captured using Beckman Coulter Gallios Flow Cytometer (Beckman Coulter, Inc. Brea, CA). Data were analyzed using Kaluza Analysis Software.

Preparation of CSE

Cigarettes used in this study were Huangshan Brand cigarettes, of which the tar, nicotine, and carbon monoxide contents were 10 mg/cigarette, 0.9 mg/cigarette, and 11 mg/cigarette, respectively. CSE was prepared by bubbling smoke from 1 cigarette into 10 ml of RPMI 1640 or DMEM (ThermoFisher, Gibco, Cat# 11965092) at a rate of 1 cigarette per 2 min, as described previously [21]. The pH of CSE was adjusted to 7.2–7.4. After being filtered through a sterile 0.22 μm filter (Merck&Millipore, Darmstadt, Germany, Cat# SLGP033R), some CSE preparation was diluted 7 times with RPMI 1640 or DMEM and used to monitor the absorbance at 320 nm (optical density of 0.67 ± 0.01). CSE was freshly prepared for each experiment and diluted with culture media immediately before use. Meanwhile, control media was prepared by bubbling air through 10 ml of culture media, adjusting pH to 7.4, and sterile filtering as described for CSE preparation.

Cell culture and treatment

All the cell lines used in this study were purchased from Procell (Wuhan, China). The human monocyte cell line THP-1 cells (RRID: CVCL_0006) were grown in RPMI 1640 medium containing 10% fetal bovine serum (FBS) (ThermoFisher, Gibco, Cat# 10100147 C) and 50 μmol/l β-mercaptoethanol. The human EC line human umbilical vein ECs (HUVECs, RRID: CVCL_2959) were cultured in RPMI 1640 medium containing 10% FBS. The human pulmonary EC line human lung microvascular endothelial cell line-5a (HULEC-5a cells) (RRID: CVCL_0A11) were cultured in MCDB131 (no L-Glutamine) (ThermoFisher, Gibco, Cat# 10372019) containing 10% FBS, 10ng/mL epidermal growth factor (EGF) (ThermoFisher, Gibco, Cat# AF-100-15), 1 mg/ml Hydrocortisone (MedChemExpress, NJ, Cat# HY-N0583), 10 mM glutamine (ThermoFisher, Gibco, Cat# A2916801). The mouse AM cell line MH-S cells (RRID: CVCL_3855) were grown in Dulbecco's Modification of Eagle's Medium (DMEM) medium containing 10% FBS and 50 μmol/l β-mercaptoethanol. The mouse EC line bEnd.3 cells (CVCL_0170) were cultured in DMEM medium containing 10% FBS. All media were supplemented with 100 μg/ml streptomycin, 100 U/ml penicillin, 0.25 μg/ml amphotericin B, and 10 mmol/l HEPES. Cells were all cultured at 37 °C in a humidified 5% CO_2 atmosphere. THP-1 cells were incubated with 100 ng/ml phorbol 12-myristate 13-acetate (PMA) (Sigma Aldrich, Cat# P8139) for 48 h to differentiate into macrophages. Liposomes were prepared for long- and very long-chain ceramide treatment as previously described [22]. Briefly, both C16-ceramide (Sigma Aldrich, Cat# 860516P) and C24-ceramide (Sigma Aldrich, Cat# 860524P) were solubilized in methanol at a concentration of 5 mM respectively and dried by nitrogen gas under vacuum to create the lipid film. To make ceramide solution, PBS supplemented with 0.3% (w/v) fatty-acid free BSA was preheated at 50 °C and then added to the lipid film, followed by vortexing and sonicating at 50 °C for 1 h. For ceramide treatment, C16-ceramide and C24-ceramide stock solutions were diluted 1:1 in serum-free RPMI 1640 or DMEM medium at different ratios for final concentrations ranging from 0.1 to 100 μM. PMA-induced THP-1 cells (hereafter referred to as "TP cells") were co-cultured with HUVECs or HULEC-5a cells and MH-S cells were co-cultured with bEnd.3 cells. Briefly, ECs (HUVECs, HULEC-5a cells, or bEnd.3 cells) were grown up to 80% confluence one day prior to being co-cultured into the lower chamber in a 24-well plate. Macrophages (TP cells or MH-S cells) were previously treated and then moved into the upper chamber of 24-well transwell inserts (0.4 μm pore size) (Merck&Millipore, Cat# PCHT24H48), which were transferred to the 24-well plate in normal hanging position to culture with ECs.

Transient transfection

Small interfering RNAs (siRNAs) were designed and synthesized by Ribobio (Guangzhou, Guangdong, China). The freeze-dried powders of siRNAs were dissolved in RNA-free water to make 20 μM storage solutions which were aliquoted and stored at -20 °C to avoid freeze/thaw cycles. For transient transfection of siRNAs, Lipofectamine RNAiMAX reagent (ThermoFisher, Invitrogen, Cat# 13778150) was mixed with siRNAs at a ratio of 8 μl:

7.5 μl mixed siRNAs storage solutions and Lipofectamine RNAiMAX reagent according to the manufacturer's protocol. To separately silence *SPTLC1*, *SPTLC2*, *CERS2*, and *CERS5*, 3 different siRNAs against each gene were separately transfected into macrophages, 2 of which with the highest interference efficiency against each gene were mixed to form 2 different tetra-combinations. Macrophages were transfected with the 2 different tetra-combinations of siRNAs to simultaneously silence *SPTLC1*, *SPTLC2*, *CERS2*, and *CERS5*. Similarly, to silence *GJA1*, HUVECs and bEnd.3 cells were transfected with siRNAs against human *GJA1* and mouse *Gja1*, respectively. Target sequences of all siRNAs against *SPTLC1*, *SPTLC2*, *CERS2*, *CERS5*, and *GJA1* used in this study were provided in Table S1.

EVs purification

EVs were isolated from the conditioned culture media of macrophages in accordance with previously described methods and guideline recommendation [23]. Briefly, media from TP cells or MH-S cells with different treatments were centrifuged at 2000 g, 4 °C for 20 min. The supernatant was centrifuged at 10,000 g, 4 °C for 30 min after being removed into new tubes. The supernatant was transferred to new tubes followed by ultracentrifugation at 100,000 g, 4 °C for 70 min. After the supernatant was removed, the EVs pellets were resuspended with ice-cold PBS. The resuspended pellets from the same cells were collected into a single centrifuge tube and were ultracentrifuged at 100,000 g, 4 °C for 70 min. After the supernatant was removed completely, the pellets were dissolved in 50 ul ice-cold PBS.

Lipidomics

For sample collection, cells and EVs should be counted to insure no less than 3×10^5 cells or 1×10^{10} particles for each sample. Cell samples and EV samples were normalized by cell counts and particle counts, respectively. For each sample, 200 μl water was added to the sample. After being frozen and thawed with liquid nitrogen for 3 times, samples were sonicated for 10 min in ice-water bath. The 480 μl extract solution (MTBE: MeOH = 5:1) containing internal standard was added to each sample. After being sonicated for another 10 min in ice-water and then incubated at -40 °C for 1 h, samples were centrifuged at 900 g, 4 °C for 15 min. With 250 μl supernatant being transferred to a fresh tube, the rest of the sample was added with 250 μl MTBE and was sonicated, incubated, and centrifuged again. Therefore another 250 μl supernatant was taken out. This step was repeated once more. A total of 750 μl combined supernatant was dried in a vacuum concentrator at 37 °C. Each of the dried samples was reconstituted in 100 μl resuspension buffer (DCM: MeOH: H_2O = 60:30:4.5), followed by sonication in ice-water bath for 10 min. Samples were then centrifuged at 16,200 g, 4 °C for 15 min and 30 μl supernatant of each sample was transferred to a fresh glass vial for LC/MS analysis. The quality control (QC) sample was prepared by mixing an equal aliquot of the supernatants from all the samples. LC-MS/MS analyses were performed using an UHPLC system (Vanquish, Thermo Fisher Scientific, Waltham, MA, USA), equipped with a Kinetex C18 column (2.1 × 100 mm, 1.7 μm, Phenomenex, Torrance, CA, USA). Finally, Biobud-v2·1·4·1 Software was employed for the quantification of the target compounds. The absolute content of individual lipids corresponding to the internal standard (IS) was calculated on the basis of peaks area and actual concentration of the identical lipid class IS.

RNA extraction and RT-PCR assay

Total RNA was extracted from cells and mouse lung homogenates using Trizol reagent (ThermoFisher, Invitrogen, Cat# 15596018CN). RNA was reverse-transcribed into cDNA with HiScript II Q RT SuperMix for qPCR (Vazyme, Nanjing, Jiangsu, China, Cat# R222-01). Quantification RT-PCR was performed using ChamQ Universal SYBR qPCR Master Mix (Vazyme, Cat# Q711-03) and Step One PlusTM Real-Time PCR System (Applied Biosystems, Foster City, CA, USA). Primers were manufactured by Genscript (Nanjing, Jiangsu, China). *RPLP0* was used as internal standard for mRNAs. Primer sequences were designed to be intron-spanning and were shown in Table S2.

Western blot analysis

Western blotting was performed as previously described [24]. Individual immunoblots were probed with mouse anti-SPTLC1 mAb (Proteintech, Wuhan, Hubei, China, Cat# 66899-1-Ig) diluted 1:1000, rabbit anti-SPTLC2 pAb (Proteintech, Cat# 51012-2-AP) diluted 1:1000, mouse anti-CERS2 mAb (Novus Biologicals, Centennial, CO, USA, Cat# H00029956-M01A) diluted 1:1000, rabbit anti-CERS5 pAb (Novus Biologicals, Cat# NBP1-76964) diluted 1:1000, rabbit anti-GJA1 pAb (Proteintech, Cat# 26980-1-AP) diluted 1:1000, rabbit anti-Calnexin pAb (Proteintech, Cat# 10427-2-AP) diluted 1:1000, rabbit anti-CD9 pAb (Proteintech, Cat# 20597-1-AP) diluted 1:1000, rabbit anti-CD81 pAb (Proteintech, Cat# 27855-1-AP) diluted 1:1000, rabbit anti-GAPDH pAb (Biogot, Nanjing, Jiangsu, China, Cat# AP0063) diluted 1:5000, mouse anti-α-Tubulin mAb (Sigma Aldrich, Cat# T5168) diluted 1:4000 in 5% (wt/vol.) non-fat dried milk in Tris-buffered saline with Tween-20 (TBST) buffer.

Immunofluorescence staining

Immunofluorescence staining on human lung tissue sections, mouse lung tissue sections, HUVECs, and bEnd.3 cells was performed as described previously [24].

Section (4 μm) from paraffin-embedded human lung samples were deparaffinized and rehydrated, followed by heat-induced epitope retrieval using HIER citrate buffer (pH 6.0). Incubation with 30% H_2O_2 was performed at room temperature to reduce the autofluorescence of human lung tissues. After being blocked with 7.5% BSA in 0.3% Triton X-100 (Sigma Aldrich, Cat# V900502) for 1 h at room temperature, cells cultured on glass coverslips and lung tissue sections were incubated with primary antibody to CD68 (1:200, Abcam, Cat# ab955), SPT (1:200, Abcam, Cat# ab307432), CerS2 (1:200, Abcam, Cat# ab315452), CerS5 (1:200, ThermoFisher, Invitrogen, Cat# PA5-98731), GJA1 (1:100, Abcam, Cat# ab230537), CD31 (1:200, Novus Biologicals, Cat# NB600-562) overnight at 4 °C. After being washed with PBS for three times, samples were incubated with the associated fluorescein (FITC)- or Cy3-conjugated secondary antibodies (1:200, Jackson ImmunoResearch, Cat# 111-165-003, 115-095-003, 111-095-003, 115-165-003) for 1 h at room temperature in the dark. Cytoskeletons were stained with FITC-Phalloidin (YEASEN, Shanghai, China, Cat# 40735ES75) for 30 min at room temperature and nuclei were stained with 4′,6-diamidino-2-phenylindole (DAPI) (Sigma Aldrich, Cat# D9542) for 5 min at room temperature. Stained sections were imaged using OLYMPUS automated fluorescence microscope BX63 (OLYMPUS, Shinjuku, Tokyo, Japan) and Zeiss LSM 710 confocal microscope (Zeiss, Oberkochen, Germany). Quantification of SPT, CerS2, and CerS5 in pulmonary macrophages as well as GJA1 in ECs in lung tissues was carried out by using cellSens softwere (OLYMPUS). Briefly, for each sample, at least 100 pulmonary macrophages marked by CD68 were counted to quantify the fluorescence intensity of SPT, CerS2, and CerS5 in pulmonary macrophages. And for each section, at least 10 randomly fields were selected for quantification of GJA1 fluorescence intensity in ECs labeled by CD31.

Enzyme-linked-immunosorbent serologic assay (ELISA)

The concentrations of TNF-α, IL-6, MMP9 (MULTI-SCIENCES, Hangzhou, Zhejiang, China, Cat# EK282, EK206, EK2M09), and SOD (Jingmei Biotech Co. Ltd., Shenzhen, China, Cat# JM-02672M1) in both mouse lung homogenates and serums were measured with ELISA Kits according to the manufacturers' instructions.

Histopathological analysis

Fresh human and mouse lung samples were fixed in 30% formalin and embedded in paraffin before sectioning (4 μm) and staining. Hematoxylin and eosin (H&E) staining was used to determine the inflammatory and emphysematous changes and Masson's trichrome staining was used to determine the severity of pulmonary fibrosis. All stained sections were scanned using Leica ScanScope CS2 (Leica Microsystems, Deerfield, IL) with its software. For quantitation of emphysema-like changes, airspace enlargement was quantified by measuring the mean linear intercept (MLI) and the destruction of alveolar walls was quantified by the destructive index (DI) as described earlier [25]. Specifically, 10 fields at a magnification of ×400 were captured for each mouse lung and were coved with a 580 μm×340 μm-grid. The total length of each line of the grid divided by the number of alveolar intercepts was defined as the MLI. A graticule with 42 points was superimposed on the lung tissue field. Points falling on alveolar and/or alveolar duct spaces were counted and structures underlying these points were classified as normal (N) and destroyed (D). If alveolar spaces and alveolar duct spaces were surrounded by intact walls opened in only one place, they were considered as normal. When an alveolar wall was disrupted in 2 or more places, when an alveolar duct space contained 2 or more islands of lung parenchyma within its lumen, or when there were more than 2 disruptions of contiguous alveoli that opened into a single duct space, D was counted. A total of 420 points were evaluated per tissue and the DI was calculated: $DI = D / (N + D) \times 100\%$. The experimenters conducting the histopathological analysis were blind to group allocation.

Apoptosis assay of alveolar septum cells

Terminal deoxynucleotidyl transferase-mediated dUTP nick-end labeling (TUNEL) was performed to label the DNA-damaged cells in situ in frozen sections of mouse lung tissues using TUNEL BrightGreen Apoptosis Detection Kit (Vazyme, Cat# A112) following the manufacturer's instructions. Labeled sections were imaged using OLYMPUS automated fluorescence microscope BX63 (OLYMPUS). For each mouse, no less than 5000 cells were counted according to nuclei stained by DAPI and the apoptotic index (AI) was calculated as the percentage of TUNEL-positive nuclei.

Measurement of pulmonary endothelial and epithelial permeability

To measure the relative impact of injury on pulmonary endothelial and epithelial barriers in vivo, Evans Blue (EB) dye extravasation assay [26] was carried out, which enabled the accumulation of Evans Blue in the airspace and interstitial compartments to be simultaneously determined. Briefly, a total of 100 μl 2% EB (YEASEN, Cat# 60528ES08) saline solution was slowly injected into the tail vein of the mouse. Mice were anesthetized and sacrificed 1 h after injection. Blood was collected from the left ventricle, followed by 1 ml BALF collection through trachea. A total of 10 ml ice-cold saline was slowly injected into the right ventricle, with the aorta below the diaphragm snipped, to remove the blood from

the perfused lung. Lung tissue was carefully dissected out from the thoracic cavity, weighted, and placed in a centrifuge tube containing 250 µl formamide (LEAGENE, Beijing, China, Cat# BZ1210) for further incubation at 55 °C for another 48 h. To measure the concentrations of EB in serum, BALF, and lung tissue, samples of blood, BALFs, and lung tissues in formamide were all centrifuged at 3000 g for 15 min at 4 °C and the supernatants were collected for further measurement. Aliquot 100 µl/well of EB standards made from EB saline solution (for serum and BALF) or formamide solution (for lung tissue extracts), samples from serum (diluted 1:10 in saline), undiluted samples of BALF, and undiluted samples of lung tissue extract in a 96-well plate. Measure absorbance of samples and EB standards at 620 nm and 740 nm using a microplate reader (Synergy 2, BioTEK instruments, Agilent, CA). The A_{620} readings were corrected by using the correction factor $y = 1.193 \times A_{740} + 0.007$ as $y \times A_{620}$. Use standards to get absolute EB concentrations in µg/ml. Lung tissue EB concentration, a reflection of injury on pulmonary endothelial barriers, was normalized by lung weight. BALF EB concentration, representing injury on both pulmonary endothelial and epithelial barriers, was divided by serum EB concentration to normalize and account for variability in the tail vein injections.

Cell migration assays

To assess the migratory ability of EC lines, 20,000 cells of each group were seeded in 400 µl serum-free medium onto an 8 µm 24-well transwell insert (Merck&Millipore, Cat# PCEP24H48) and cell migration was performed in the presence of 600 µl 10% FBS complete medium in the lower chamber of 24-well plate. After 24 h, media were removed and the polycarbonate filters with the migrated cells were fixed and stained with crystal violet (Beyotime, Shanghai, China, Cat# C0121). The migrated cells of each sample were counted in ten randomly selected fields.

FITC-dextran transwell permeability assay

To assess the endothelial permeability, HUVECs or bEnd.3 cells of each group were seeded onto the top of the filter membrane in a 0.4 µm 24-well tranwell insert (Merck&Millipore, Cat# PCHT24H48). After the monolayers of cells formed, media in both upper and lower chambers was replenished by fresh complete media with FITC-dextran (Sigma Aldrich) being added only into the medium of upper chambers additionally to reach a final concentration of 50 µg/ml. Fluorescence of the media in the lower chambers was measured by Synergy™ 2 multi-mode microplate readers (BioTek, Vineland, NJ, USA) with excitation at 485 nm and emission at 535 nm 24 h after incubation. The endothelial permeability is reflected by the fluorescence value of media from lower chamber due to the trans-monolayer of ECs permeation of FITC-dextran.

Sample Preparation for transmission electron microscopy (TEM) imaging

For cells, no less than 10^6 cells were freshly collected in a tube and centrifuged at 1500 rpm, 4 °C for 5 min. Cell pellets were fixed with 2.5% glutaraldehyde and then washed thrice with phosphate buffer. Samples were post-fixed in 1% osmic acid at 4 °C for 2 h followed by deionized water rinsing thrice. After being stained in 1% uranyl acetate for 2 h, samples were serially dehydrated in 50%, 70%, 90%, 100% ethyl alcohol and 100% acetone. After dehydration, samples were embedded in EPON 812 resin. Embedded samples were put in thermotank at 37 °C, 45 °C, and 60 °C for 12 h, 12 h, and 48 h, respectively. For EVs, 20 µl freshly purified EVs sample was loaded on copper electron microscopy grids. All the samples were negatively labeled with uranyl acetate solution for 2 min. After being washed thrice with PBS, the grids were put on filter paper under a semi-dry conditions. Both cell samples and EVs samples were imaged using FEI Tecnai G2 TEM (FEI, Hillsboro, Victoria, OR, USA).

Nanoparticle tracking analysis (NTA)

NTA was carried out to measure the size distribution and concentration of EVs with ZetaView PMX 110 (Particle Metrix, Meerbusch, Germany). Isolated EV samples were appropriately diluted using PBS. NTA measurement was recorded and analyzed at 11 positions. The ZetaView system was calibrated using 110 nm polystyrene particles. Temperature was maintained around 22 °C.

PKH26 staining and tracing

Both macrophages and EVs were labeled with the PKH26 fluorescent cell linker (Sigma Aldrich, Cat# MINI26) at ambient temperature (20 °C-25 °C) according to the manufacturer's protocol. Briefly, for macrophages, a total of 2×10^7 cells were collected and washed once using medium without serum followed by centrifugation at 400 g for 5 min. The cell pellet was resuspended by 1 ml Diluent C and rapidly mixed with 1 ml 4 µM PKH26 solution. After incubating for 5 min, the staining was stopped by 2 ml FBS. Cells were centrifuged at 400 g for 10 min and resuspend as well as transferred to a fresh tube in 10 ml complete medium. After centrifugation at 400 g for 5 min, cells pellet was washed 2 more times with 10 ml complete medium to ensure removal of unbound dye. Finally, stained macrophages were resuspended in complete medium and co-cultured with ECs. To tracing PKH26-stained EVs derived from macrophages as well as EVs derived from PKH26-stained macrophages in ECs, both HUVECs and bEnd.3 cells were directly fixed, stained with DAPI and analyzed under microscopy. For

EVs, no less then 2×10^{11} EVs were collected and resuspended by 1 ml Diluent C and rapidly mixed with 1 ml 4 μM PKH26 solution. After incubating for 5 min, the staining was stopped by 1% BSA. In in vitro experiments, EVs were centrifuged at 100,000 g for 70 min at 4 °C and resuspend in conditioned culture media for HUVECs and bEnd.3 cells for incubation with these cells. In in vivo experiments, EVs were centrifuged at 100,000 g for 70 min at 4 °C and resuspend in normal saline (NS) to produce a final concentration of 5×10^8 EVs/μl. The EVs or NS were intratracheally injected to mouse (1×10^9 EVs/g). After 24 h and 48 h, harvested lung tissues were successively fixed in 4% paraformaldehyde, embedded in OCT, cut into 4 μm thick sections, and stained with DAPI for further assessment under microscopy.

Animal study

MH-S cells were treated with or without 5% CSE for 24 h, of which the conditioned media were collected and centrifuged to isolate EVs (MH-S-Ctrl-EVs or MH-S-CSE-EVs). Male C57BL/6J mice of 8 weeks were randomly divided into 3 groups and intratracheally injected with normal saline (NS), MH-S-Ctrl-EVs or MH-S-CSE-EVs (1×10^9 EVs/g), respectively. Half mice of every group were exposed to CS and the other half to room air (Air) for 1 h per day on day 1 and day 2 after EVs administration. After 6 cycles, CS/Air-exposure time for each mouse was extended to 2 h per day. Mouse lung tissues were harvested another 14 days later for histopathological analysis and further experiments. The size of every group of mice was decided based on the 3R principle (Reduction, Replacement, Refinement). For each experimental group, there were no exclusions. The experimenters conducting the injection and CS exposure were all blind to these 3 injection groups.

Statistical analysis

Statistical analyses were performed using Prism GraphPad 9.0 Software. Quantitative data are presented as mean ± standard deviation (SD). Normality of data distribution was assessed using the Shapiro-Wilk test. For comparisons between two groups, a Student's t-test was use. Comparisons among three or more groups were performed using one-way ANOVA for parametric data, followed by Bonferroni's multiple comparisons test. For non-parametric data, the Kruskal-Wallis test was used, followed by Dunn's multiple comparisons test. A P-value of < 0.05 was considered statistically significant. All results are based on at least three independent experiments.

Results

CS influences the expression of enzymes involved in ceramide biosynthesis in macrophages

Our previous human lung tissues scRNA-seq dataset (GSE171541) [15] showed that genes encoding enzymes involved in de novo synthesis of ceramides were generally upregulated in pulmonary macrophages from smokers and COPD patients (Fig. S1A). Heatmap analysis revealed that a distinct subset of macrophages from smokers exhibited a general increase in these genes, which was particularly pronounced in COPD lungs (Fig. 1A and B). The UMAP plots of pulmonary macrophages (Fig. S1B-S1D) further illustrated that the high expression of *SPTLC1*, *SPTLC2*, *CERS2*, and *CERS5* was more pronounced in macrophages from smokers, suggesting a potential link between ceramide biosynthesis and smoking. Reanalysis of other scRNA-seq datasets of human lung tissues (GSE173896, EGAS00001004244) and bulk RNA-seq datasets of human AMs (GSE13896, GSE130928, GSE183983) revealed that the expression of ceramide biosynthesis enzymes tended to be higher in smokers and COPD patients compared to non-smokers, although these differences did not always reach statistical significance (Fig. S2A-S2C). In addition, we confirmed this sphingolipid metabolic reprogramming in AMs from CS-exposed mice and CSE-treated human macrophages (differentiated from THP-1 monocytes, hereafter referred to as TP cells) as well as mouse AM cell line MH-S cells by qPCR (Fig. 1C and D, Fig. S2D-S2F). Immunofluorescence staining of lung sections from smokers and COPD patients showed increased expression of both enzymes SPT and CerS (including CerS2 and CerS5) in pulmonary macrophages marked by CD68 (Fig. 1E). Furthermore, in CSE-treated macrophages, these enzymes were upregulated in a dose-dependent manner at both the mRNA (Fig. 1D) and protein levels (Fig. 1F and G). Interestingly, this upregulation persisted even after CSE removal, indicating a sustained metabolic reprogramming in macrophages, similar to what was observed in ex-smokers (Fig. S2B).

CS-induced enzymes upregulation increases ceramide de novo synthesis in macrophages

To assess whether this enzymes upregulation translates into increased ceramide production, we performed lipidomic analysis on TP and MH-S cells. The composition of ceramide species was similar between the two cell types, with C24-ceramide being the most abundant, followed by C16-ceramide (Fig. 2A). In response to CSE treatment, total ceramide content significantly increased in a dose-dependent manner, accompanied by elevated levels of triglycerides (TAGs) and fatty acids (FAs) that give rise to fatty acyl CoAs, essential substrates for de novo ceramide synthesis (Fig. S3A and S3B). Notably,

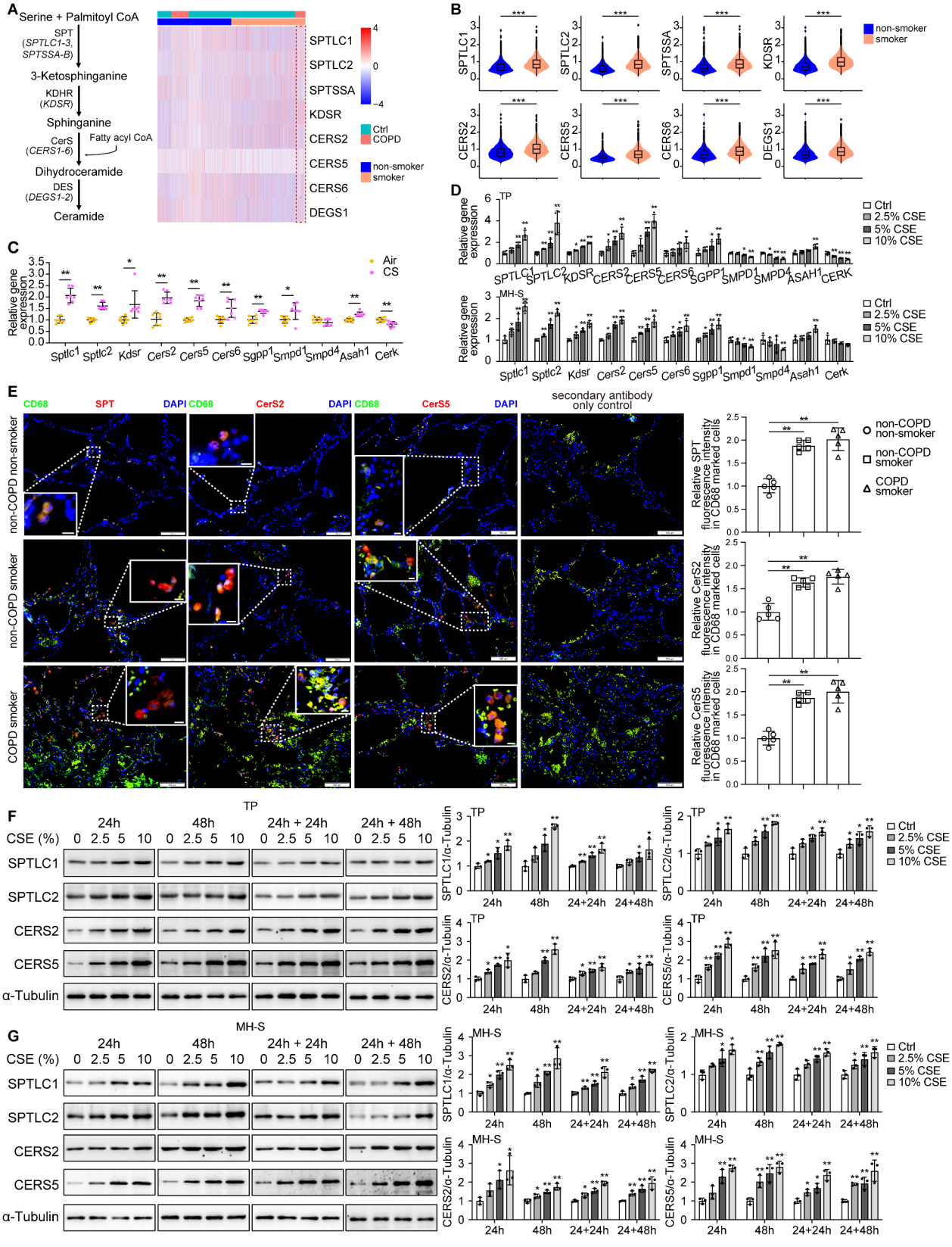

Fig. 1 (See legend on next page.)

(See figure on previous page.)

Fig. 1 CS influences the expression of enzymes involved in ceramide biosynthesis in macrophages. (**A**) Schematic depiction of the de novo synthesis pathway of ceramides (left). SPT, serine palmitoyltransferase; KDHR, 3-ketodihydrosphingosine reductase; CerS, ceramide synthase; DES, dihydroceramide desaturase. Heatmap showing the expression levels of genes encoding enzymes implicated in the de novo synthesis pathway of ceramides in macrophages from our previous scRNA-seq dataset of human lung tissues (GSE171541) (right). (**B**) Violin plots showing the expression distributions of genes that encode enzymes involved in the de novo synthesis of ceramides in pulmonary macrophages among non-smokers and smokers in dataset GSE171541. ***$P < 2.2e-12$ vs. non-smoker. (**C**) Eight-week-old C57BL/6 mice were exposed to cigarette smoke (CS) or room air (Air) for 6 months. $n = 7$. The mRNA levels of *Sptlc1*, *Sptlc2*, *Kdsr*, *Cers2*, *Cers5*, *Cers6*, *Sgpp1*, *Smpd1*, *Smpd4*, *Asah1*, and *Cerk* were measured by qPCR in the AMs isolated from each mouse. *$P < 0.05$ and **$P < 0.01$ vs. Air. (**D**) Macrophages differentiated from THP-1 (TP cells, up) and mouse AMs cell line, MH-S cells (bottom) were treated with or without different doses of CSE for 24 h, when the mRNA levels of *SPTLC1*, *SPTLC2*, *KDSR*, *CERS2*, *CERS5*, *CERS6*, *SGPP1*, *SMPD1*, *SMPD4*, *ASAH1*, and *CERK* of both cells were measured by qPCR. $n = 4$. *$P < 0.05$ vs. Ctrl, **$P < 0.01$ vs. Ctrl. (**E**) Immunofluorescence staining of lung sections from non-smokers and smokers with or without COPD. CD68 (green) marks macrophages, while SPT and CerS (red) indicate the expression of ceramide biosynthesis enzymes. The secondary antibody control shows nonspecific fluorescence, mainly from erythrocytes, which was excluded during quantification. Scale bars = 100 μm (for enlarged areas in white solid boxes, Scale bars = 10 μm). $n = 5$. **$P < 0.01$ vs. non-COPD non-smoker. (**F**, **G**) TP cells (**F**) and MH-S cells (**G**) were treated with or without different doses of CSE for 24 h (24 h) or 48 h (48 h), and a part of macrophages treated with CSE for 24 h were cultured in normal medium for another 24 h (24 h + 24 h) or 48 h (24 h + 48 h). The protein levels of SPTLC1, SPTLC2, CERS2, and CERS5 in all these cells were measured by western blotting. $n = 3$. *$P < 0.05$ and **$P < 0.01$ vs. Ctrl at the same time point

both C24- and C16-ceramides, the most abundant species, showed the greatest elevation after CSE exposure (Fig. 2B and C).

Next, we used siRNA-mediated silencing of *SPTLC1*, *SPTLC2*, *CERS2*, and *CERS5* (Fig. S3C and S3D) to confirm their role in ceramide production stimulated by CS. Simultaneously silencing these four genes significantly reduced both mRNA and protein levels of the targeted enzymes upregulated by CS (Fig. 2D and E). Consequently, the total ceramide levels, particularly C24- and C16-ceramides, together with C14- and C22-ceramides, were markedly decreased (Fig. 2F and G), which corresponded well to the preferential catalytic action of CerS2 and CerS5 in the biosynthesis of C22-C24-ceramides and C14- as well as C16-ceramides, respectively [10, 27]. These results confirmed that CS-induced ceramide synthesis in macrophages relies on the upregulation of *SPTLC1*, *SPTLC2*, *CERS2*, and *CERS5*.

Metabolic communication between macrophages and ECs reduces *GJA1* expression in ECs

Building on our previous findings that sphingolipid metabolic reprogramming in macrophages is linked to endothelial dysfunction, with gap junction of endothelial cell (EC) being a predicted target [15], we examined the effects of macrophage-derived ceramides on *GJA1* expression in ECs. *GJA1* that encodes connexin43 (Cx43), a key component of gap junctions in pulmonary endothelial barriers, was significantly downregulated in ECs from smokers and COPD patients, based on scRNA-seq data and immunostaining of human lung sections (Fig. 3A and C and Fig. S4A-S4C). This suggests that *GJA1* expression is sensitive to smoking-induced metabolic alterations.

In a co-culture system of macrophages (TP or MH-S cells) and ECs (HUVECs, HULEC-5a or bEnd.3 cells) (Fig. 3D), we found that CSE-treated macrophages dose-dependently reduced *GJA1* expression in ECs, even after CSE was removed (Fig. 3E and F, and Fig. S4D-S4F), which was consistent with the sustained upregulation of *SPTLC1*, *SPTLC2*, *CERS2*, and *CERS5* in macrophages after CSE being withdrawn (Fig. 1F and G). Interestingly, CSE alone did not directly affect *GJA1* expression in ECs, nor did it stimulate ceramide synthesis in ECs through de novo pathway (Fig. S4G-S4I). However, treating ECs with a mixture of C16- and C24-ceramides in the range of concentrations that did not affect EC viability (Fig. S4J) recapitulated the effect of co-culturing with CSE-treated macrophages, reducing *GJA1* expression in a dose-dependent manner (Fig. 3G and H, Fig. S4K, and S4L). Furthermore, *SPTLC1*, *SPTLC2*, *CERS2*, and *CERS5* silencing in macrophages reversed the CSE-induced reduction of *GJA1* in co-cultured ECs (Fig. 3I and J, and Fig. S4M-S4O), supporting the hypothesis that ceramides from macrophages mediate the metabolic communication leading to reduced *GJA1* expression in ECs.

Ceramide-mediated metabolic communication impairs EC barrier integrity and migration

Considering the role of *GJA1* in maintaining the structural and functional integrity of endothelium [28], we next investigated the effects of ceramide-mediated metabolic communication on EC function. When co-cultured with CSE-treated macrophages, ECs exhibited significantly increased permeability and impaired migration compared to those that co-cultured with control macrophages (Fig. 4A and B, Fig. S5A, and S5B). Direct treatment of ECs with CSE (Fig. 4C and D) or ceramides (Fig. 4E and F, Fig. S5C, and S5D) alone also increased permeability and inhibited migration, although the effects were less pronounced than in the co-culture system, indicating that the indirect effects of macrophage-derived ceramides play a major role in exacerbating endothelial dysfunction. When *SPTLC1*, *SPTLC2*, *CERS2*, and *CERS5* were silenced in CSE-treated macrophages, the hyperpermeability and impaired migration of co-cultured ECs were partially reversed (Fig. 4G and H, Fig. S5E, and S5F), further supporting the role of ceramide-mediated metabolic communication. Furthermore, silencing *GJA1*

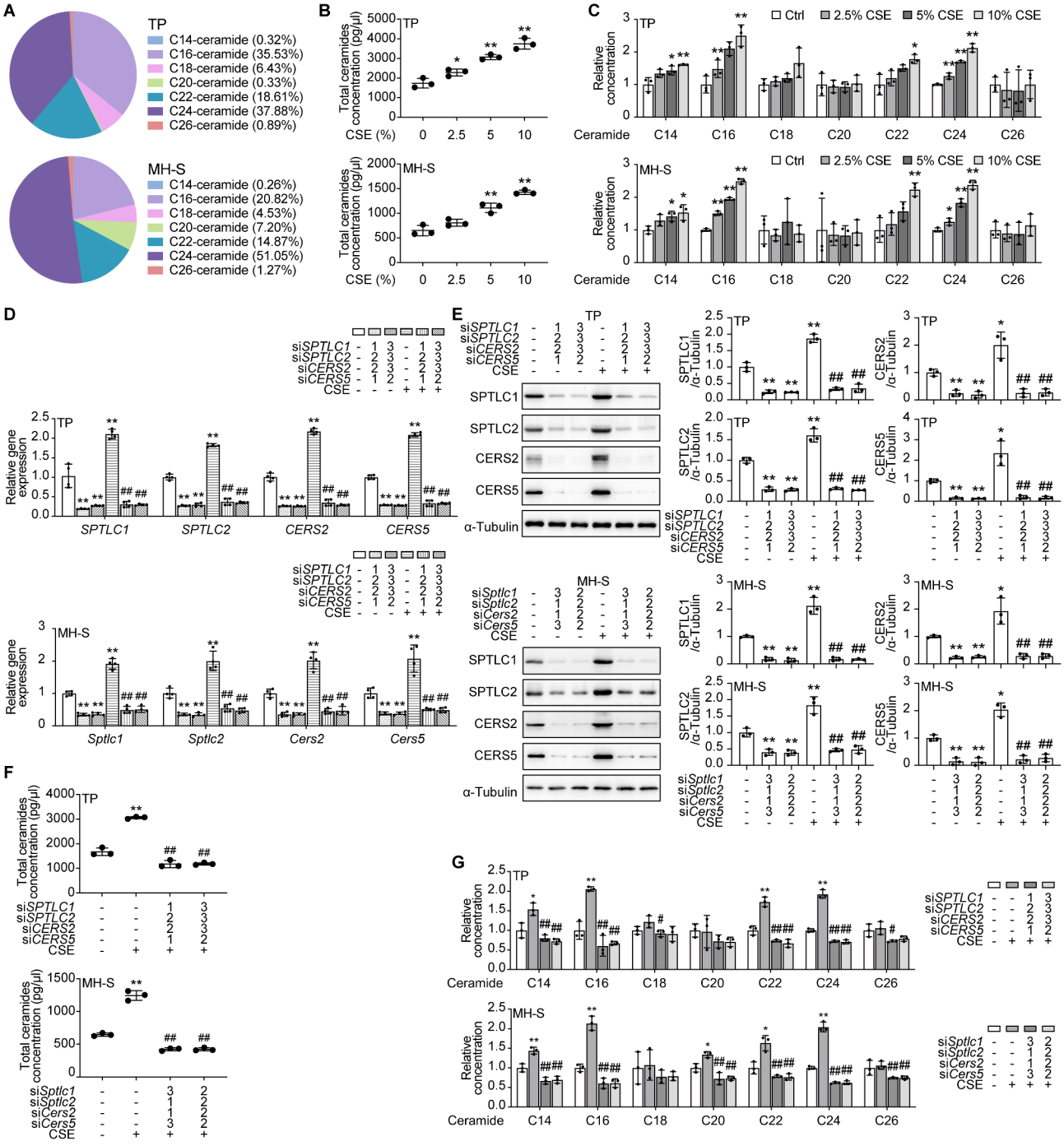

Fig. 2 CS-induced enzymes upregulation increases ceramide de novo synthesis in macrophages. (**A**-**C**) TP cells and MH-S cells were treated with or without different doses of CSE for 24 h when quantitative lipidomic analysis were performed. (**A**) The pie charts showing the composition of ceramides in control TP cells (up) and control MH-S cells (bottom). The dot plots and the bar plots showing the concentrations of total ceramides (**B**) and the relative concentrations of each species of ceramides (**C**) respectively in TP cells (up) and MH-S cells (bottom) treated with or without different doses of CSE for 24 h. $n = 3$. $^{*}P < 0.05$ and $^{**}P < 0.01$ vs. Ctrl. (**D**-**G**) Both TP cells (up) and MH-S cells (bottom) were transfected with or without 2 different mixtures of siRNAs against *SPTLC1*, *SPTLC2*, *CERS2*, and *CERS5* for 48 h and then treated with or without 5% CSE. After another 24 h, the mRNA levels of *SPTLC1*, *SPTLC2*, *CERS2*, and *CERS5* in TP cells and MH-S cells were measured by qPCR (**D**), meanwhile quantitative lipidomic analysis was performed, and after another 48 h, western blot was carried out to measure the protein levels of SPTLC1, SPTLC2, CERS2, and CERS5 in TP cells and MH-S cells (**E**). The dot plots and the bar plots showing the concentrations of total ceramides (**F**) and the relative concentrations of each species of ceramides (**G**) respectively in TP cells and MH-S cells of each group. $n = 3$. $^{*}P < 0.05$ and $^{**}P < 0.01$ vs. siNC without CSE, $\#P < 0.05$ and $\#\#P < 0.01$ vs. siNC with CSE

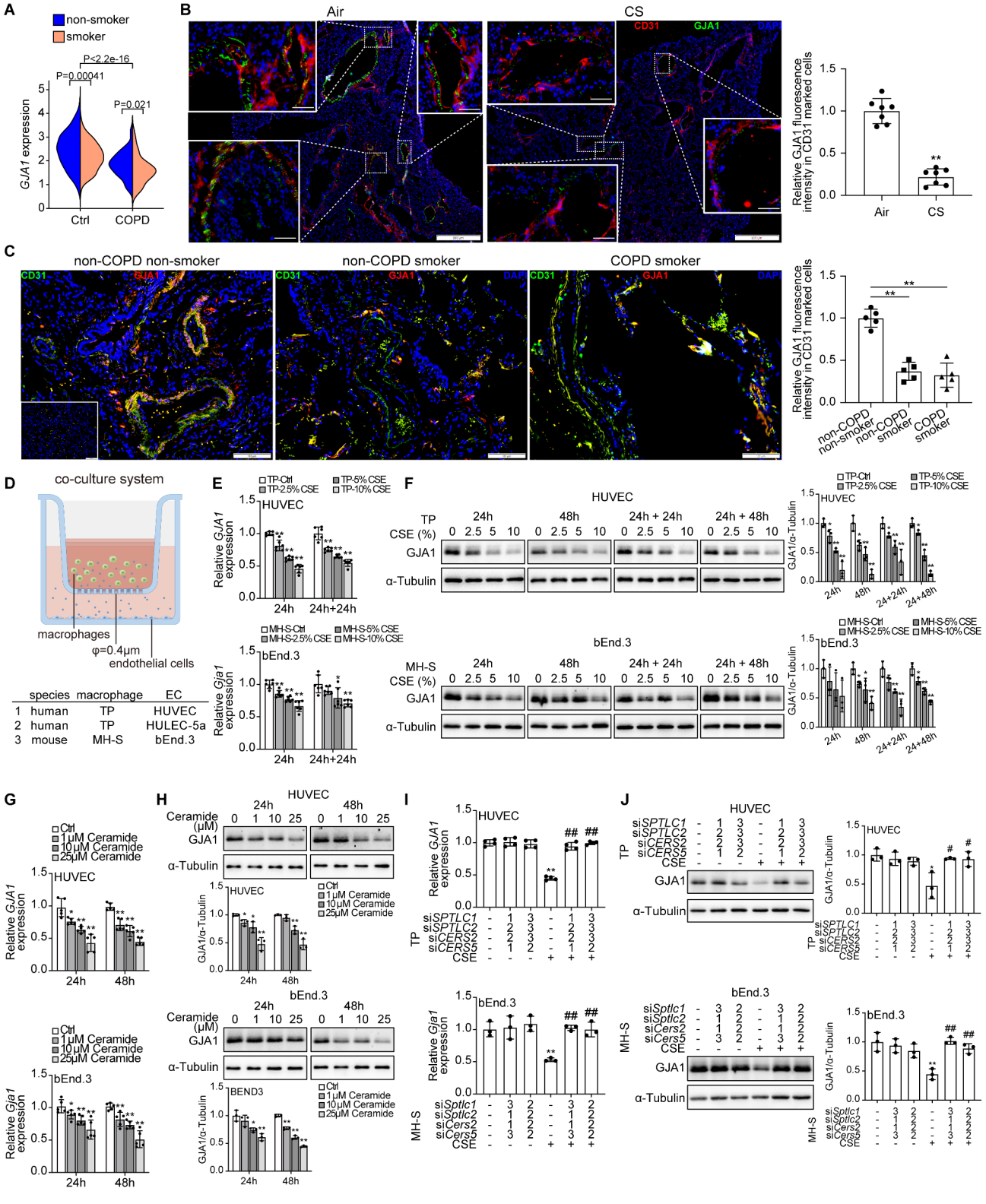

Fig. 3 (See legend on next page.)

(See figure on previous page.)

Fig. 3 Metabolic communication between macrophages and ECs reduces *GJA1* expression in ECs. (**A**) Split violin plot showing the expression distributions of *GJA1* in pulmonary endothelial cells among control and COPD patients with different smoking histories in dataset GSE171541. (**B**) The protein levels of CD31 (red) and GJA1 (green) in cigarette smoke (CS)- or room air (Air)-exposed C57BL/6 mice for 6 months were measured by immunofluorescence staining (Scale bars = 500 μm, for enlarged areas in white dotted boxes, Scale bars = 50 μm). $n = 7$. $^{**}P < 0.01$ vs. Air. (**C**) The protein levels of CD31 (green) and GJA1 (red) in human lung tissues from non-smoker without COPD and smokers with or without COPD were measured by immunofluorescence staining. The secondary antibody only control was displayed in the white solid box at bottom left corner of the first image. Scale bars = 100 μm. $n = 5$. $^{**}P < 0.01$ vs. non-COPD non-smoker. (**D**) Schematic of the macrophages-endothelial cells co-culture system. Human macrophages (TP cells) were seeded in the upper chamber of 0.4 μm pore-sized transwell inserts and co-cultured with human ECs (HUVECs or HULEC-5a cells) grown in the lower chambers of the plate. Similarly, mouse macrophages (MH-S cells) were co-cultured with mouse ECs (bEnd.3 cells) using the same transwell system. (**E**-**H**) TP cells and MH-S cells treated with or without different doses of CSE for 24 h were co-cultured with HUVECs and bEnd.3 cells respectively in the presence (24 h–48 h) or absence (24 h + 24 h–24 h + 48 h) of CSE for another 24 h–48 h. The mRNA (**E**, $n = 6$) and protein (**F**, $n = 3$) levels of *GJA1* in HUVECs and bEnd.3 cells were measured. $^{*}P < 0.05$ and $^{**}P < 0.01$ vs. TP/MH-S-Ctrl at the same time point. HUVECs and bEnd.3 cells were treated with or without mixtures of C16- and C24-ceramides in equal proportions at different concentrations for 24–48 h. The mRNA (**G**, $n = 5$) and protein (**H**, $n = 3$) levels of *GJA1* were measured. $^{*}P < 0.05$ and $^{**}P < 0.01$ vs. Ctrl at the same time point. (**I**, **J**) Both TP cells and MH-S cells transfected with or without 2 different mixtures of siRNAs against *SPTLC1*, *SPTLC2*, *CERS2*, and *CERS5* for 48 h were treated with or without 5% CSE for another 24 h, and then co-cultured with HUVECs and bEnd.3 cells for 24 h, respectively. The mRNA (**I**, $n = 4$ of HUVECs, $n = 3$ of bEnd.3 cells) and protein (**J**, $n = 3$) levels of *GJA1* in HUVECs and bEnd.3 cells were measured. $^{*}P < 0.05$ and $^{**}P < 0.01$ vs. TP/MH-S-siNC without CSE, $\#P < 0.05$ and $\#\#P < 0.01$ vs. TP/MH-S-siNC with CSE

in ECs alone was sufficient to induce hyperpermeability and migration inhibition (Fig. 4I and K), indicating that ceramide-mediated *GJA1* downregulation is a key mechanism underlying the observed endothelial dysfunction.

Macrophage-derived EVs deliver ceramides to ECs

Next, we sought to determine whether EVs facilitate the transfer of ceramides from macrophages to ECs. Displaying cup-like shape under transmission electron microscopy (TEM) (Fig. 5A) with typical EVs markers (CD9 and CD81) (Fig. 5B), macrophage-derived EVs were larger and more numerous in response to CSE treatment as characterized by nanoparticle tracking analysis (NTA) (Fig. 5C), suggesting enhanced EV production under CSE stimulation. Further examination by TEM revealed the presence of early endosome- and MVB-like ultrastructures related to EVs synthesis and secretion [29] in CSE-treated TP cells (Fig. S6A-S6D). They also harbored more lipid droplets than control cells (Fig. S6E) and large aggregates of enlarged and swollen mitochondria with abnormal cristae and reduced electron density (Fig. S6F). Lipidomic analysis showed that EV ceramide composition closely matched that of their parent macrophages, with C16- and C24-ceramides being the most abundant species (Fig. 5D). CSE treatment significantly enhanced the total ceramide content in EVs, with pronounced increases in C14-, C16-, C22-, and C24-ceramides, which were largely abrogated by silencing *SPTLC1*, *SPTLC2*, *CERS2*, and *CERS5* in macrophages (Fig. 5E and F).

To determine whether EVs from macrophages could be taken up by ECs, we labeled both macrophage-derived EVs and macrophages with PKH26, a fluorescent dye, and co-cultured them with unlabeled ECs, respectively. The red fluorescence signal observed in ECs confirmed that macrophage-derived EVs were internalized by ECs (Fig. 5G, Fig. S6G, and S6H).When unlabeled ECs was co-cultured with labeled macrophages under the condition of CSE treatment (Fig. 5H, Fig. S6I, and S6J), this EV uptake was dose-dependent on CSE exposure and persisted even after the removal of CSE (Fig. 5I and Fig. S6K-S6M), suggesting a sustained potential for intercellular ceramide transfer.

When assessing the effects of macrophage-derived EVs on EC function, we found that ECs incubated with EVs isolated from CSE-treated macrophages exhibited a decline in *GJA1* expression, with increased permeability and decreased migration, all of which were partially reversed by reduced the ceramide load in EVs via silencing *SPTLC1*, *SPTLC2*, *CERS2*, and *CERS5* in macrophages (Fig. 6A and D, and Fig. S7A). Additionally, to confirm that the observed effects were due to ceramides carried by EVs rather than potential CSE residue, we ultracentrifuged conditioned media containing CSE alone (without macrophages), which had no impact on *GJA1* expression or EC function (Fig. S7B-S7E). Together, these findings establish that CSE-stimulated macrophage-derived EVs deliver ceramides to ECs, highlighting a crucial pathway of metabolic communication that links macrophage lipid metabolism to endothelial dysfunction in COPD.

Macrophage-derived EVs exacerbate CS-triggered COPD in vivo

To investigate the role of macrophage-derived EVs in vivo, we administered PKH26-labeled EVs from CSE-treated MH-S cells to CS-exposed mice. EVs were readily taken up by pulmonary ECs (Fig. 7A and B, and Fig. S8A). CS exposure alone reduced *GJA1* expression in pulmonary ECs, and this effect was amplified when mice were injected with CSE-treated macrophage-derived EVs (MH-S-CSE-EVs) (Fig. 7C and D). Histological analysis revealed that CS-exposed mice receiving MH-S-CSE-EVs exhibited severe emphysema-like changes, including airspace enlargement, alveolar wall destruction, and increased cell apoptosis (Fig. 7E and I). In line with these findings, the permeability of pulmonary endothelial

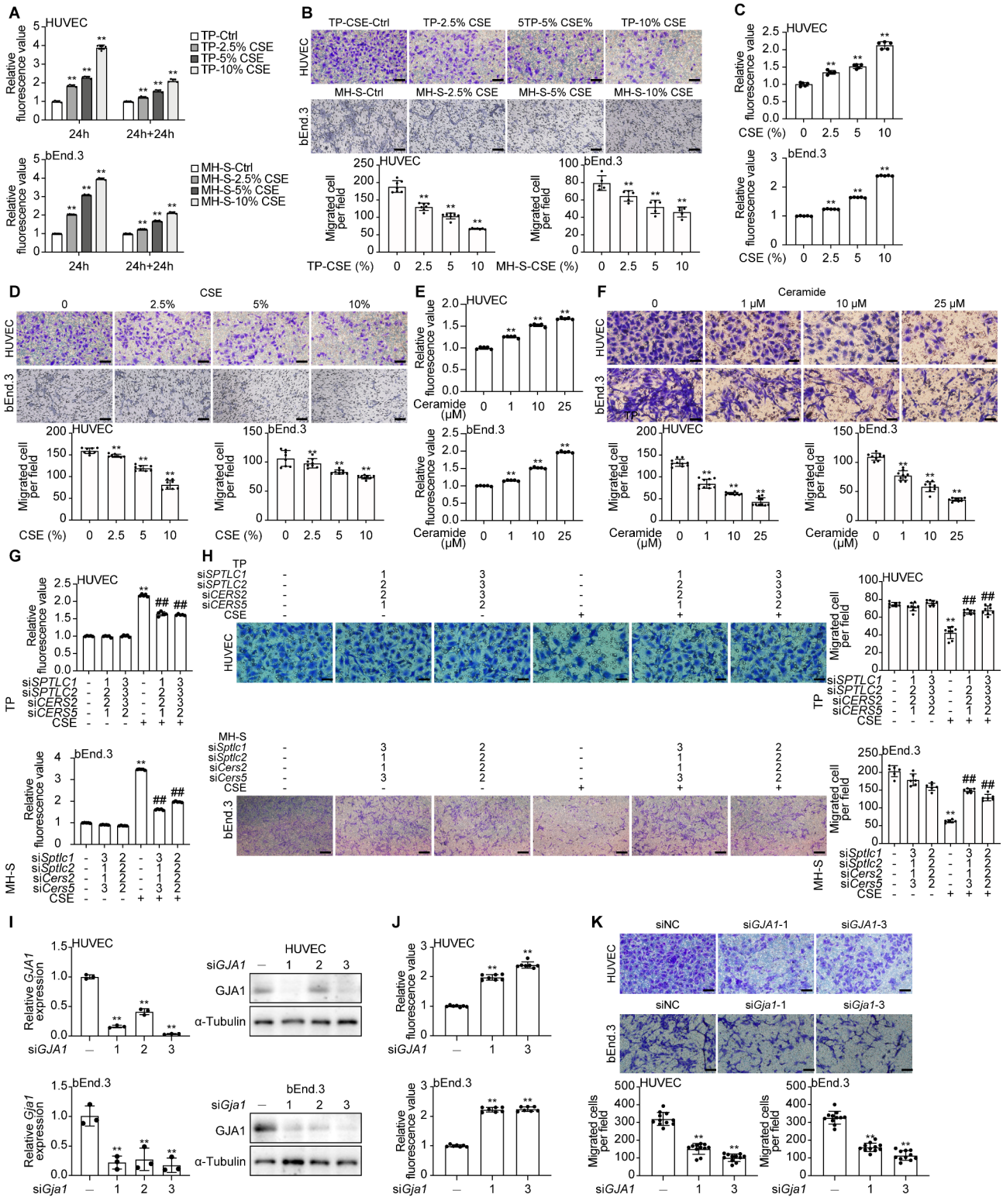

Fig. 4 (See legend on next page.)

(See figure on previous page.)

Fig. 4 Ceramide-mediated metabolic communication impairs EC barrier integrity and migration. (**A**, **B**) TP cells and MH-S cells treated with or without different doses of CSE for 24 h were co-cultured with HUVECs and bEnd.3 cells respectively in the presence (24 h) or absence (24 h + 24 h) of CSE for another 24 h. (**A**) The permeability of HUVECs and bEnd.3 cells were assessed by FITC-dextran transwell permeability assay. $n = 5$. $^{**}P < 0.01$ vs. TP/MH-S-Ctrl at the same time point. (**B**) Meanwhile, the migration of co-cultured HUVECs and bEnd.3 cells in the presence of CSE for another 24 h were analyzed by transwell assay. Scale bars = 100 μm. $n = 7$ of HUVECs, $n = 5$ of bEnd.3 cells. $^{**}P < 0.01$ vs. TP/MH-S-Ctrl at the same time point. (**C**-**F**) HUVECs and bEnd.3 cells were treated with or without different doses of CSE (**C**, **D**) or mixtures of C16- and C24-ceramides in equal proportions at different concentrations (**E**, **F**) for 24 h when permeability (**C**, **E***n* = 5) and migration (**D**, Scale bars = 100 μm, $n = 8$; **F**, Scale bars = 50 μm, $n = 10$ of HUVECs, $n = 9$ of bEnd.3 cells) were assessed. $^{*}P < 0.05$ and $^{**}P < 0.01$ vs. Ctrl. (**G**, **H**) HUVECs and bEnd.3 cells were co-cultured with 5%CSE-treated *SPTLC1*, *SPTLC2*, *CERS2*, and *CERS5*-silenced TP cells and MH-S cells that were treated with or without 5%CSE for another 24 h. After 24 h, permeability (**G**, $n = 5$) and migration (**H**, for HUVECs, Scale bars = 50 μm; for bEnd.3 cells, Scale bars = 100 μm; $n = 8$ of HUVECs, $n = 6$ of bEnd.3 cells) were assessed. $^{**}P < 0.01$ vs. TP/MH-S-siNC without CSE, $^{\#\#}P < 0.01$ vs. TP/MH-S-siNC with CSE. (**I**) HUVECs and bEnd.3 cells were transfected with or without 3 different pieces of siRNAs against *GJA1* for 48 h, when the mRNA and protein levels of *GJA1* in HUVECs and bEnd.3 cells were measured. $n = 3$. $^{**}P < 0.01$ vs. siNC. (**J**, **K**) HUVECs and bEnd.3 cells were transfected with or without the 2 pieces of siRNAs against *GJA1* with the highest interference efficiency for 48 h, when the permeability (**J**, $n = 7$) and migration (**K**, Scale bars = 100 μm; $n = 11$) were assessed. $^{**}P < 0.01$ vs. siNC

barriers, measured by Evans Blue (EB) dye retention in lung tissue, was significantly higher in mice receiving MH-S-CSE-EVs (Fig. 7J). This was accompanied by elevated EB and protein concentrations in BALFs (Fig. 7K and L), further indicating epithelial barrier damage. Moreover, pulmonary inflammation, tissue remodeling, and oxidative stress were exacerbated in mice receiving MH-S-CSE-EVs (Fig. S8B-S8D). Collectively, EVs derived from CSE-treated macrophages facilitate COPD development in mice triggered by CS.

Discussion

Here, we identified a mechanism by which CS disrupts the pulmonary endothelial barrier through EVs-mediated metabolic communication between pulmonary macrophages and ECs. CS exposure drives sphingolipid metabolic reprogramming in pulmonary macrophages, resulting in the de novo synthesis of long- and very long-chain ceramides. These ceramides are packaged into EVs and delivered to ECs, where they impair endothelial integrity and function, contributing to COPD development.

Although ceramide elevation in CS-exposed lungs has been widely documented, the mechanisms underlying this increase across different cell types remain debated [8, 10, 30–32]. In this study, we used enzyme expression as a proxy for metabolic flux and found that CS exposure led to a robust and general upregulation of high-abundance enzymes responsible for de novo ceramide synthesis in pulmonary macrophages, which strongly suggests that CS enhances ceramide biosynthesis through this pathway in macrophages. Supporting this, simultaneous silencing of *SPTLC1*, *SPTLC2*, *CERS2*, and *CERS5* counteracted CSE-induced ceramide increases, particularly in C16-, C22-, and C24-ceramides—species preferentially catalyzed by CerS2 and CerS5 [27]. These findings clarify that CS promotes de novo synthesis of long- and very long-chain ceramides in pulmonary macrophages primarily by upregulating these key enzymes. Several transcriptomic studies have linked sphingolipid metabolic reprogramming with mitochondrial function in AMs [11, 12, 15], and our observation of morphologically abnormal mitochondria in CSE-treated macrophages supports this association. Given the central role of mitochondria in metabolic sensing and regulation [33, 34], future investigations exploring mitochondrial involvement in CS-induced sphingolipid metabolic reprogramming in macrophages may offer deeper insights into metabolic regulation in the immunopathogenesis of COPD.

In our study, labeled EVs administered intratracheally were found to target ECs, supporting their role in endothelial barrier disruption mediated by ceramides. However, it is important to note that pulmonary macrophages are not restricted to the alveolar spaces. Macrophages residing in the pulmonary mesenchyme and vasculature may deliver EVs directly to ECs [35, 36], thereby bypassing the alveolar epithelium and providing a more direct route for EV-mediated communication. To some extent, our in vivo experiment more closely simulated the physiological conditions under which AM-derived EVs interact with ECs in the lung. However, the precise mechanisms by which EVs from AMs reach ECs in the lung are still not fully understood. One possible route is transcellular transport [37–39], where EVs are internalized by epithelial cells through endocytosis and subsequently released on the basolateral side via exocytosis to reach adjacent cells or even tissues. Another potential route is paracellular transport [38, 40], which is more likely to occur during COPD development due to CS-induced damage that disrupts integrity of alveolar epithelium [41]. This increased permeability could allow EVs to move between cells, facilitating their passage from AMs to the endothelium.

The effects of increased ceramides vary across different cell types in the lung. While causing apoptosis of alveolar epithelial cells and ECs [30, 31], ceramides dampen AM efferocytosis [10], which in turn aggravates pulmonary inflammation resulting from accumulation of apoptotic cells. Although the ceramides detected in human plasma [6, 42], BALFs [10], and lung tissues [42] are predominantly long-, very long-, and ultra-long-chain ceramides, most studies have not thoroughly examined the distinct

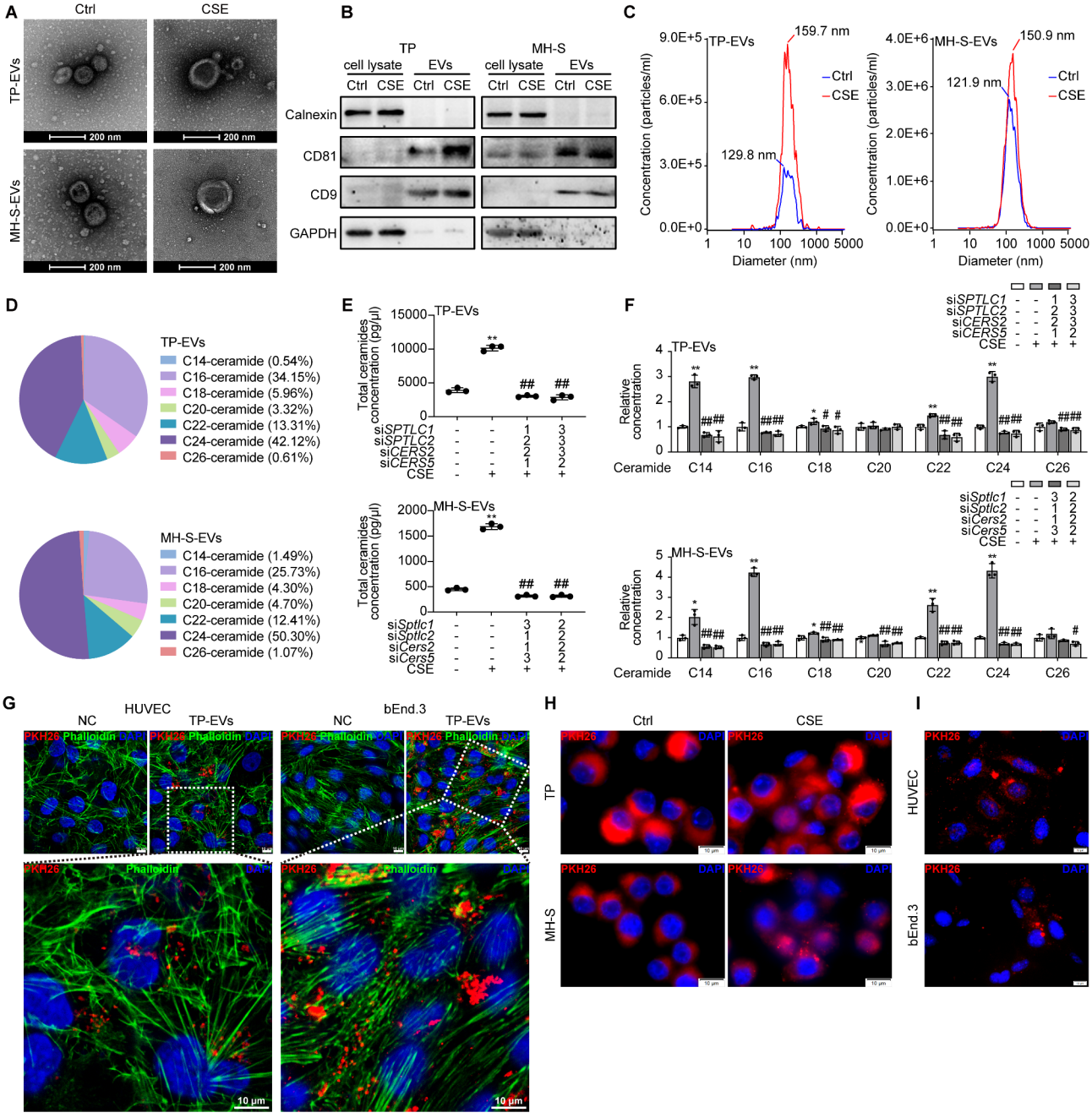

Fig. 5 Macrophage-derived EVs deliver ceramides to ECs. (**A**) TEM images of the EVs obtained from the conditioned medium of control and CSE-treated TP cells and MH-S cells. Scale bars = 200 nm. (**B**) Western blot analysis of EVs markers (CD9, CD81), endoplasmic reticulum marker (Calnexin), and GAPDH in EVs and cell lysates of TP cells and MH-S cells treated with or without 5% CSE. (**C**) The size distributions of the EVs from TP cells and MH-S cells treated with (red line) or without (blue line) 5% CSE were measured by NTA. Quantitative lipidomic analysis of the EVs derived from *SPTLC1*, *SPTLC2*, *CERS2*, and *CERS5*-silecned TP cells and MH-S cells that were treated with or without 5% CSE for another 24 h. (**D**) The pie charts showing the composition of ceramides in the EVs from control TP cells (up) and MH-S cells (bottom). (**E**, **F**) The dot plots and the bar plots showing the concentrations of total ceramides (**E**) and the relative concentrations of each species of ceramides (**F**) respectively in EVs from TP cells (up) and MH-S cells (bottom) of each group. $n = 3$. $^{*}P < 0.05$ and $^{**}P < 0.01$ vs. siNC without CSE, $\#P < 0.05$ and $\#\#P < 0.01$ vs. siNC with CSE. (**G**) PKH26-labeled EVs (red) derived from 5% CSE-treated TP cells and MH-S cells (TP/MH-S-EVs) were incubated with HUVECs (left) and bEnd.3 cells (right) for 12 h, respectively, whereas those incubated with EVs-depleted PHK26 solution served as the negative control (NC). The areas circled by white boxes in the top confocal micrographs were enlarged and displayed below, with the cytoskeletons being labeled by FITC-Phalloidin (green). Scale bars = 10 μm. (**H**, **I**) Both TP cells and MH-S cells were marked with PKH26 followed by incubation with or without 5% CSE. Some TP cells and MH-S cells were directly fixed and analyzed under microscopy (**H**, Scale bars = 10 μm), whereas the rest TP cells were co-cultured with unlabeled HUVECs and the rest MH-S cells were co-cultured with bEnd.3 cells for another 24 h, respectively. Afterwards, both HUVECs and bEnd.3 cells were fixed and analyzed under microscopy (**I**, Scale bars = 10 μm)

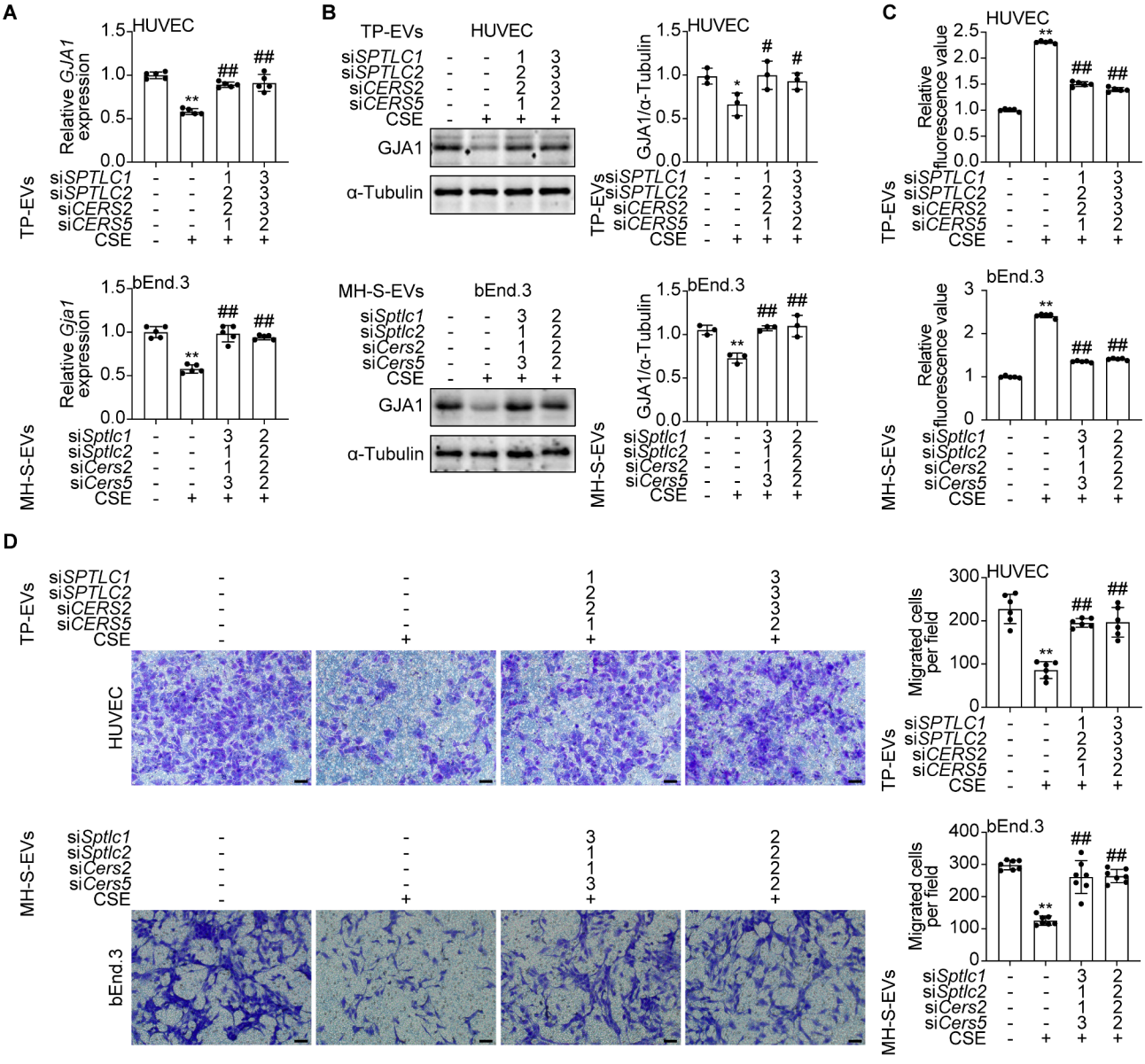

Fig. 6 EV-delivered ceramides reduce *GJA1* expression and impair EC function. (**A**-**D**) Both TP cells and MH-S cells transfected with or without 2 different mixtures of siRNAs against *SPTLC1*, *SPTLC2*, *CERS2*, and *CERS5* for 48 h were treated with or without 5% CSE for another 24 h, followed by EVs isolation. HUVECs (up) and bEnd.3 cells (bottom) were incubated with the EVs from different groups of TP cells and MH-S cells for 24 h, respectively, when the mRNA (**A**, $n=5$) as well as protein (**B**, $n=3$) levels of *GJA1*, the permeability (**C**, $n=5$), and migration (**D**, Scale bars = 100 μm; $n=6$ of HUVECs, $n=7$ of bEnd.3 cells) of HUVECs and bEnd.3 cells were measured. $^{**}P<0.01$ vs. TP/MH-S-siNC without CSE, $^{\#\#}P<0.01$ vs. TP/MH-S-siNC with CSE

effects of different ceramide species on various lung cell types. Generally, the longer the acyl chains, the stronger the hydrophobicity of the ceramides [43] and the greater reliance of their transport on vesicles [27]. In our study, C16- and C24-ceramides, the most significantly elevated ceramide species in CSE-treated pulmonary macrophages and their EVs, were shown to disrupt pulmonary endothelial barriers. This finding highlights a paracrine mechanism through which ceramides act as transcellular signals, mediating metabolic communication between macrophages and ECs. Our data aligns with previous reports documenting elevated EV levels in BALFs from smokers [44] and CS-exposed macrophages [45] suggesting that ceramide-mediated inward budding of MVBs and the subsequent release of ceramide-enriched EVs [4, 5] may play a critical role in this process.

Emerging evidence points to the ceramide/protein phosphatase 2 A (PP2A) axis [46, 47], which has been shown to inhibit *GJA1* expression and impair gap junctions in other tissues [48], raising the possibility that this pathway may also contribute to *GJA1* downregulation in the pulmonary endothelium during COPD development.

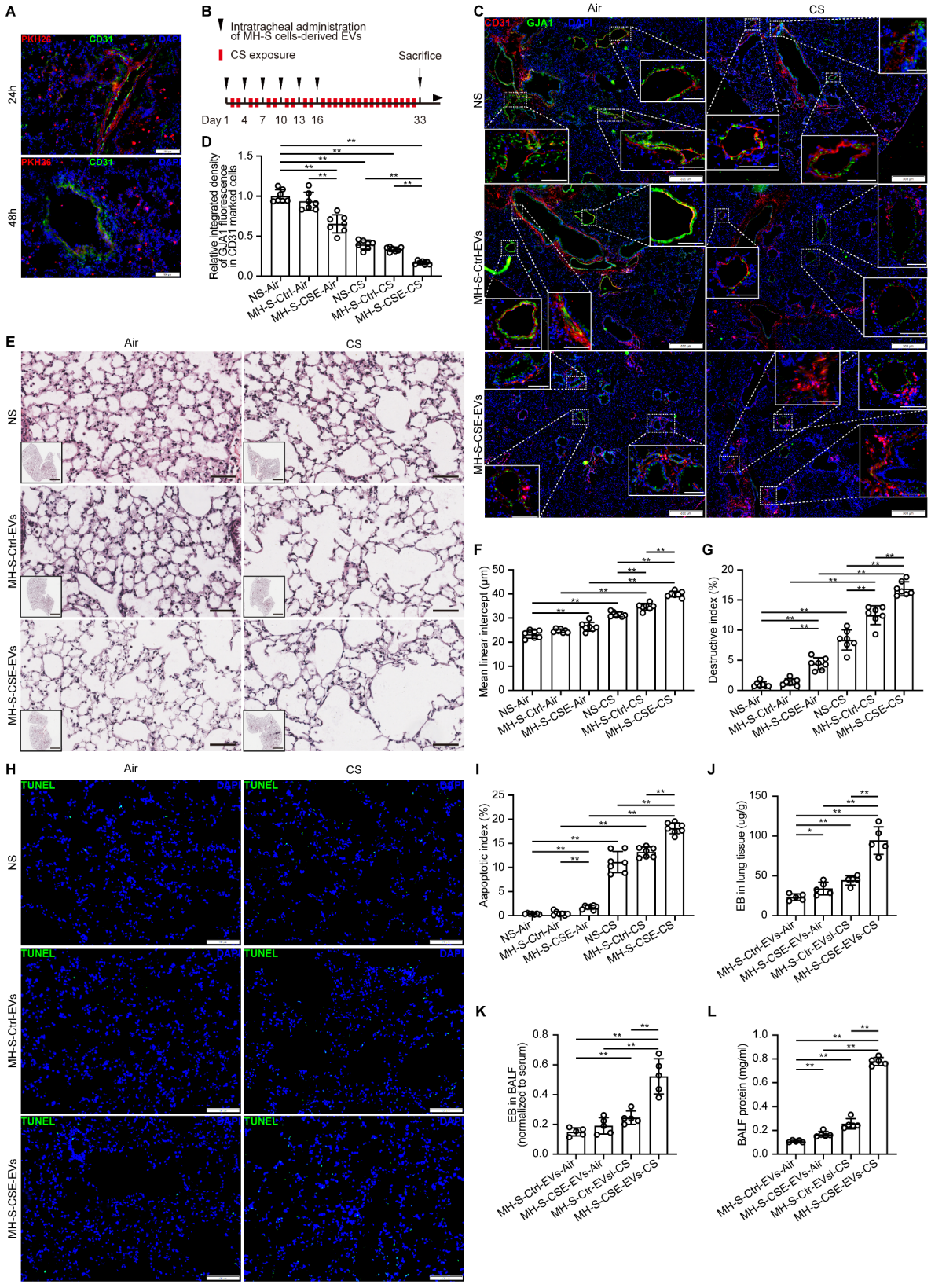

Fig. 7 (See legend on next page.)

(See figure on previous page.)

Fig. 7 Macrophage-derived EVs stimulated by CSE exacerbate CS-triggered COPD in mice. (**A**) Eight-week-old mice were intratracheally injected with 1×10^9 particles/g PKH26 (red)-labeled EVs isolated from conditioned culture media of MH-S cells. Lung tissues were dissected 24 h (up) and 48 h (bottom) after injection ($n = 3$ for each time point) and stained with DAPI (blue) and CD31 (green) (Scale bars = 100 μm). (**B**-**I**) Eight-week-old C57BL/6 mice intratracheally injected with normal saline (NS) or EVs isolated from conditioned culture media of control MH-S cells (MH-S-Ctrl-EVs) or 5% CSE-treated MH-S cells (MH-S-CSE-EVs) were exposed to room air (Air) or cigarette smoke (CS) as diagramed in the schematic protocol. $n = 7$ (**B**). (**C**) The protein levels of CD31 (red) and GJA1 (green) in these mice lungs were measured by immunofluorescence staining (Scale bars = 500 μm; for enlarged areas in the white solid boxes, Scale bars = 50 μm). (**D**) The expression levels of GJA1 in ECs were quantified as the integrated density of GJA1 fluorescence in CD31 marked cells. (**E**) The representative Haematoxylin and Eosin (H&E) staining images of mice lung tissues from every group were displayed (Scale bars = 60 μm; for the full-scan of each lung tissue in the black solid box, Scale bars = 2 mm). Mean linear intercept (MLI) (**F**) and destructive index (DI) (**G**) were measured to assess the alveolar space and destruction of alveolar walls of mice lung tissues from every group. (**H**) The representative in situ TUNEL (green) staining images with all cell nuclei being stained with DAPI (blue) of mice lung tissues from every group were displayed (Scale bars = 100 μm). (**I**) For each mouse, no less than 5000 cells were counted to calculate the apoptotic index (AI) as the percentage of TUNEL-positive nuclei. $^*P < 0.05$ and $^{**}P < 0.01$. (**J**-**L**) Another set of mice ($n = 5$) were subjected to the same treatments as described in (**B**). Lung extravasation of Evans blue (EB) dye were assessed (**J**). BALFs were collected for assessment of BALF EB dye concentration (**K**) and protein concentration (**L**). $^*P < 0.05$ and $^{**}P < 0.01$

Future studies are needed to explore this potential axis and its impact on endothelial function. Here, we found that *GJA1*-silenced ECs exhibited hyperpermeability and impaired migration, suggesting the downregulation of *GJA1*, which encodes connexin43 (Cx43), may mediate the damaging effects of ceramides on ECs. As essential components of gap junctions that enable adjacent cells to communicate both electrically and chemically, connexins have been found to regulate vascular remodeling [49], function [50], and interaction with immune cells [51, 52] in both channel-dependent and -independent manners. Cx43 has been reported to maintain the endothelial barrier function [53] and promote EC migration [54] via interactions with tight junction proteins and tyrosine phosphatase, respectively. In HeLa cells, Cx43 was found to interact with p21-activated protein kinase 1 (PAK1) and thus activate the p38 MAP kinase responsible for cytoskeletal actin dynamic, underpinning the role of Cx43 in the control of migratory activity by filopodia formation [55]. Additionally, given the modulatory effect of Cx43 on angiogenic factors vascular endothelial growth factor (VEGF) production [56], downregulation of *GJA1* may weaken the regenerative capacity of ECs in COPD pathogenesis. Together, these mechanisms underscore the multifaceted role of *GJA1* in endothelial homeostasis and highlight it as a potential target in therapeutic strategies for COPD.

The metabolic communication between pulmonary macrophages and ECs, mediated by the intercellular delivery of ceramides via EVs, reflects the metabolic plasticity of macrophages. This may represent a survival strategy for pulmonary macrophages, enabling them to offload the lipotoxicity of accumulated triglycerides (TAGs) and fatty acids (FAs) in response to CS, however, at the cost of propagating proinflammatory ceramides [57] and hence the aggravation of pulmonary inflammation. Notably, consistent with the persistent inhibition of AM efferocytosis and the increase in ceramides reported by Petrusca et al. even 24 h after removal of AMs from the CS-containing media [10], our findings show that EV-delivered ceramides continue to exert damaging effects on ECs even after CSE withdrawal. This persistent impact may be a possible reason for the disease progression in some COPD patients after smoking cessation [58]. Therefore, targeting the ceramide synthesis pathway or the transport of long- and very long-chain ceramides through EVs may offer novel strategies to help restore pulmonary endothelial barrier integrity and reduce systemic inflammation. Future studies should explore the development of inhibitors that either suppress ceramide biosynthesis in macrophages or prevent the release of ceramide-laden EVs, offering potential for both disease modification and COPD prevention.

There are several limitations in our present study. First, due to the high cell quantity required for existing EVs extraction and measurement techniques, we were unable to perform in vitro experiments using EVs directly derived from primary human pulmonary macrophages. The use of cell lines, while informative, may not fully replicate the behavior of primary macrophages in vivo, and future studies should validate these findings in primary cells. Second, while we demonstrated that ceramide-laden EVs disrupt endothelial barrier function, we did not directly measure intracellular ceramide concentrations in ECs after treatment. Quantifying intracellular levels of C16- and C24-ceramides using mass spectrometry-based lipidomics would provide more direct evidence of ceramide uptake and its correlation with the observed biological effects. Additionally, based on the method for preparation of ceramide: cholPC described in a recent study [57], future studies should explore the use of ceramide: cholPC (cholesterol-phosphatidylcholine) mixtures to further enhance ceramide solubility and cellular uptake in future experiments. Third, while GW4869 is widely used as an EV inhibitor by blocking ceramide-mediated MVB formation as a noncompetitive neutral sphingomyelinase (N-SMase) inhibitor [59], we opted to silence key enzymes in the de novo ceramide biosynthesis pathway instead of using GW4869 for fear of its potential impact on ceramides synthesized via sphingomyelinase pathway. The third limitation lies in the choice of EVs from CSE-treated wild-type MH-S

cells for in vivo experiments, rather than using EVs from ceramide synthesis enzymes-silenced MH-S cells treated with CSE. Although EVs with reduced ceramide levels would provide a more direct validation of this metabolic communication in vivo, they might still contain other pro-inflammatory factors induced by CSE exposure, complicating the interpretation of results. Given that our in vitro findings have already confirmed that ceramide-enriched EVs from CSE-treated macrophages can damage ECs, the use of EVs from CSE-treated wild-type macrophages in vivo could partially implicate the detrimental role of ceramides delivered by EVs in exacerbating lung injury and endothelial barrier dysfunction. Future studies should attempt to refine this approach by selectively targeting ceramide synthesis while minimizing the confounding influence of other CSE-induced factors in EVs. Lastly, while our study focused on the direct impact of ceramide-loaded EVs on endothelial barrier function, future investigations should explore the potential influence of this metabolic communication on the immunomodulatory properties of ECs [60] as well as the systemic effects of these EVs on other pulmonary cell types to fully elucidate their contribution to COPD pathogenesis.

Conclusions

In summary, we establish a mechanistic model of COPD pathogenesis from the perspective of immunometabolism and intercellular communication, revealing how ceramide-laden EVs arise from sphingolipid metabolic reprogramming in pulmonary macrophages and shuttle as proinflammatory signals to disrupt the endothelial barrier. Our findings thus highlight promising new directions for COPD therapeutic intervention focused on maintaining pulmonary endothelial barrier homeostasis by targeting key enzymes, metabolites, and EVs to block aberrant metabolic communication in disease.

Abbreviations

CS	Cigarette Smoke
ECs	Endothelial Cells
COPD	Chronic Obstructive Pulmonary Disease
AMs	Alveolar Macrophages
CSE	Cigarette Smoke Extract
EVs	Extracellular Vesicles
C1P	Ceramide-1-Phosphate
S1P	Sphingosine-1-Phosphate
scRNA-seq	single-cell RNA-sequencing
UMIs	Unique Molecular Identifiers
GEO	Gene Expression Omnibus
EGA	European Genome-phenome Archive
TPM	Total Particulate Matter
CO	Carbon Monoxide
Ppm	Parts per Million
BALFs	Bronchoalveolar Lavage Fluids
BSA	Bovine Serum Albumin
FBS	Fetal Bovine Serum
HUVECs	Human Umbilical Vein Endothelial Cells
PMA	Phorbol 12-Myristate 13-Acetate
siRNAs	small interfering RNAs
IS	Internal Standard
DAPI	4′,6-Diamidino-2-Phenylindole
H&E	Hematoxylin and Eosin
MLI	Mean Linear Intercept
DI	Destructive Index
TUNEL	Terminal Deoxynucleotidyl Transferase-Mediated dUTP Nick-End Labeling
AI	Apoptotic Index
EB	Evans Blue
TEM	Transmission Electron Microscopy
NTA	Nanoparticle Tracking Analysis
NS	Normal Saline
SD	Standard Deviation
SPT	Serine Palmitoyl-CoA Transferase
CerS	Ceramide Synthase
TAGs	Triglycerides
Fas	Fatty Acids
Cx43	Connexin43
PP2A	Protein Phosphatase 2 A
PAK1	p21-Activated Protein Kinase 1
VEGF	Vascular Endothelial Growth Factor
N-SMase	Neutral Sphingomyelinase

Supplementary Information

The online version contains supplementary material available at https://doi.org/10.1186/s12964-025-02125-y.

Supplementary Material 1

Supplementary Material 2

Acknowledgements

The authors would like to thank Xiaosu Li, a freelance translator in Beijing, China, for editorial assistance.

Author contributions

Qiqing Huang and Jianqing Wu conceived and designed this study. Qiqing Huang, Tutu Kang, Shaoran Shen, Lele Liu, and Lili Zhang performed experiments. Xiaoli Zou and Qiqing Huang carried out the analysis. Qiqing Huang and Jiangqing Wu interpreted the results. Qiqing Huang and Jiangqing Wu drafted and revised the manuscript. Qiqing Huang, Xiaoli Zou, and Jianqing Wu accessed and verified the data. Qiqing Huang and Jiangqing Wu were responsible for the decision to submit the manuscript. Jianqing Wu funded and supervised the study. All authors reviewed the manuscript and approved the final version of the manuscript.

Funding

This study was supported by research grants from the National Natural Science Foundation of China under grant 82471605, 82171576, and Jiangsu Province Capability Improvement Project through Science, Technology and Education under grant No. CXZX202228 to Jianqing Wu.

Data availability

No datasets were generated or analysed during the current study.

Declarations

Ethics approval and consent to participate

All experiments involving human tissues were approved by the Ethics Committee at the First Affiliated Hospital of Nanjing Medical University (2021-SR-335). All procedures followed were in accordance with the ethical standards of the responsible committee on human experimentation (institutional and national) and with the Helsinki Declaration of 1975, as revised in 2008 (5). Informed consent was obtained from all patients for being included in the study. All animal experiments were approved by the Institutional Animal Care and Use Committee at Nanjing Medical University and complied with the ARRIVE guidelines.

Consent for publication

Not applicable.

Competing interests
The authors declare no competing interests.

Author details
[1]Key Laboratory of Geriatrics of Jiangsu Province, Department of Geriatrics, The First Affiliated Hospital of Nanjing Medical University, 300 Guangzhou Road, Nanjing, Jiangsu 210029, China

Received: 14 November 2024 / Accepted: 24 February 2025
Published online: 07 March 2025

References

1. Law BA, Liao X, Moore KS, Southard A, Roddy P, Ji R, Szulc Z, Bielawska A, Schulze PC, Cowart LA. Lipotoxic very-long-chain ceramides cause mitochondrial dysfunction, oxidative stress, and cell death in cardiomyocytes. FASEB J. 2018;32:1403–16.
2. Hannun YA, Obeid LM. Sphingolipids and their metabolism in physiology and disease. Nat Rev Mol Cell Biol. 2018;19:175–91.
3. Chakinala RC, Khatri A, Gupta K, Koike K, Epelbaum O. Sphingolipids in COPD. Eur Respir Rev. 2019;28.
4. Horbay R, Hamraghani A, Ermini L, Holcik S, Beug ST, Yeganeh B. Role of ceramides and lysosomes in extracellular vesicle biogenesis, cargo sorting and release. Int J Mol Sci. 2022;23.
5. Elsherbini A, Qin H, Zhu Z, Tripathi P, Wang G, Crivelli SM, Spassieva SD, Bieberich E. Extracellular vesicles containing Ceramide-Rich platforms: mobile raft isolation and analysis. Methods Mol Biol. 2021;2187:87–98.
6. Bowler RP, Jacobson S, Cruickshank C, Hughes GJ, Siska C, Ory DS, Petrache I, Schaffer JE, Reisdorph N, Kechris K. Plasma sphingolipids associated with chronic obstructive pulmonary disease phenotypes. Am J Respir Crit Care Med. 2015;191:275–84.
7. Berdyshev EV, Serban KA, Schweitzer KS, Bronova IA, Mikosz A, Petrache I. Ceramide and sphingosine-1 phosphate in COPD lungs. Thorax. 2021.
8. Schweitzer KS, Hatoum H, Brown MB, Gupta M, Justice MJ, Beteck B, Van Demark M, Gu Y, Presson RG Jr., Hubbard WC, et al. Mechanisms of lung endothelial barrier disruption induced by cigarette smoke: role of oxidative stress and ceramides. Am J Physiol Lung Cell Mol Physiol. 2011;301:L836–846.
9. Petrusca DN, Van Demark M, Gu Y, Justice MJ, Rogozea A, Hubbard WC, Petrache I. Smoking exposure induces human lung endothelial cell adaptation to apoptotic stress. Am J Respir Cell Mol Biol. 2014;50:513–25.
10. Petrusca DN, Gu Y, Adamowicz JJ, Rush NI, Hubbard WC, Smith PA, Berdyshev EV, Birukov KG, Lee CH, Tuder RM, et al. Sphingolipid-mediated Inhibition of apoptotic cell clearance by alveolar macrophages. J Biol Chem. 2010;285:40322–32.
11. O'Beirne SL, Kikkers SA, Oromendia C, Salit J, Rostmai MR, Ballman KV, Kaner RJ, Crystal RG, Cloonan SM. Alveolar macrophage immunometabolism and lung function impairment in smoking and chronic obstructive pulmonary disease. Am J Respir Crit Care Med. 2020;201:735–9.
12. Bassler K, Fujii W, Kapellos TS, Dudkin E, Reusch N, Horne A, Reiz B, Luecken MD, Osei-Sarpong C, Warnat-Herresthal S, et al. Alveolar macrophages in early stage COPD show functional deviations with properties of impaired immune activation. Front Immunol. 2022;13:917232.
13. Fujii W, Kapellos TS, Bassler K, Handler K, Holsten L, Knoll R, Warnat-Herresthal S, Oestreich M, Hinkley ER, Hasenauer J et al. Alveolar macrophage transcriptomic profiling in COPD shows major lipid metabolism changes. ERJ Open Res. 2021;7.
14. Liegeois M, Bai Q, Fievez L, Pirottin D, Legrand C, Guiot J, Schleich F, Corhay JL, Louis R, Marichal T, et al. Airway macrophages encompass transcriptionally and functionally distinct subsets altered by smoking. Am J Respir Cell Mol Biol. 2022;67:241–52.
15. Huang Q, Wang Y, Zhang L, Qian W, Shen S, Wang J, Wu S, Xu W, Chen B, Lin M, et al. Single-cell transcriptomics highlights immunological dysregulations of monocytes in the pathobiology of COPD. Respir Res. 2022;23:367.
16. Kyomoto Y, Kanazawa H, Tochino Y, Watanabe T, Asai K, Kawaguchi T. Possible role of airway microvascular permeability on airway obstruction in patients with chronic obstructive pulmonary disease. Respir Med. 2019;146:137–41.
17. Minet C, Vivodtzev I, Tamisier R, Arbib F, Wuyam B, Timsit JF, Monneret D, Borel JC, Baguet JP, Levy P, et al. Reduced six-minute walking distance, high fat-free-mass index and hypercapnia are associated with endothelial dysfunction in COPD. Respir Physiol Neurobiol. 2012;183:128–34.
18. Ozaki K, Hori T, Ishibashi T, Nishio M, Aizawa Y. Effects of chronic cigarette smoking on endothelial function in young men. J Cardiol. 2010;56:307–13.
19. Hisata S, Racanelli AC, Kermani P, Schreiner R, Houghton S, Palikuqi B, Kunar B, Zhou A, McConn K, Capili A et al. Reversal of emphysema by restoration of pulmonary endothelial cells. J Exp Med. 2021;218.
20. Zhang Y, Li X, Grassme H, Doring G, Gulbins E. Alterations in ceramide concentration and pH determine the release of reactive oxygen species by Cftr-deficient macrophages on infection. J Immunol. 2010;184:5104–11.
21. Yang SR, Yao H, Rajendrasozhan S, Chung S, Edirisinghe I, Valvo S, Fromm G, McCabe MJ Jr., Sime PJ, Phipps RP, et al. RelB is differentially regulated by IkappaB Kinase-alpha in B cells and mouse lung by cigarette smoke. Am J Respir Cell Mol Biol. 2009;40:147–58.
22. Honda A, Nozumi M, Ito Y, Natsume R, Kawasaki A, Nakatsu F, Abe M, Uchino H, Matsushita N, Ikeda K, et al. Very-long-chain fatty acids are crucial to neuronal Polarity by providing sphingolipids to lipid rafts. Cell Rep. 2023;42:113195.
23. Thery C, Amigorena S, Raposo G, Clayton A. Isolation and characterization of exosomes from cell culture supernatants and biological fluids. Curr Protoc Cell Biol. 2006;Chap. 3:Unit 3 22.
24. Huang Q, Chen Y, Shen S, Wang Y, Liu L, Wu S, Xu W, Zhao W, Lin M, Wu J. Klotho antagonizes pulmonary fibrosis through suppressing pulmonary fibroblasts activation, migration, and extracellular matrix production: a therapeutic implication for idiopathic pulmonary fibrosis. Aging. 2020;12:5812–31.
25. Lee JH, Hanaoka M, Kitaguchi Y, Kraskauskas D, Shapiro L, Voelkel NF, Taraseviciene-Stewart L. Imbalance of apoptosis and cell proliferation contributes to the development and persistence of emphysema. Lung. 2012;190:69–82.
26. Smith P, Jeffers LA, Koval M. Measurement of lung vessel and epithelial permeability in vivo with Evans blue. Methods Mol Biol. 2021;2367:137–48.
27. Hernandez-Corbacho MJ, Salama MF, Canals D, Senkal CE, Obeid LM. Sphingolipids in mitochondria. Biochim Biophys Acta Mol Cell Biol Lipids. 2017;1862:56–68.
28. Sedovy MW, Leng X, Leaf MR, Iqbal F, Payne LB, Chappell JC, Johnstone SR. Connexin 43 across the vasculature: gap junctions and beyond. J Vasc Res. 2022;1:13.
29. Raposo G, Stoorvogel W. Extracellular vesicles: exosomes, microvesicles, and friends. J Cell Biol. 2013;200:373–83.
30. Yang Y, Uhlig S. The role of sphingolipids in respiratory disease. Ther Adv Respir Dis. 2011;5:325–44.
31. Filosto S, Castillo S, Danielson A, Franzi L, Khan E, Kenyon N, Last J, Pinkerton K, Tuder R, Goldkorn T. Neutral Sphingomyelinase 2: a novel target in cigarette smoke-induced apoptosis and lung injury. Am J Respir Cell Mol Biol. 2011;44:350–60.
32. Petrache I, Natarajan V, Zhen L, Medler TR, Richter AT, Cho C, Hubbard WC, Berdyshev EV, Tuder RM. Ceramide upregulation causes pulmonary cell apoptosis and emphysema-like disease in mice. Nat Med. 2005;11:491–8.
33. Liu Y, Birsoy K. Metabolic sensing and control in mitochondria. Mol Cell. 2023;83:877–89.
34. Picard M, Shirihai OS. Mitochondrial signal transduction. Cell Metab. 2022;34:1620–53.
35. Wang X, Yao F, Yang L, Han D, Zeng Y, Huang Z, Yang C, Lin B, Chen X. Macrophage extracellular vesicle-packaged miR-23a-3p impairs maintenance and angiogenic capacity of human endothelial progenitor cells in neonatal hyperoxia-induced lung injury. Stem Cell Res Ther. 2024;15:295.
36. Ye J, Liu X. Macrophage-Derived small extracellular vesicles in multiple diseases: biogenesis, function, and therapeutic applications. Front Cell Dev Biol. 2022;10:913110.
37. Cain JW, Seo H, Bumgardner K, Lefevre C, Burghardt RC, Bazer FW, Johnson GA. Pig conceptuses utilize extracellular vesicles for interferon-gamma-mediated paracrine communication with the endometriumdagger. Biol Reprod. 2024;111:174–85.
38. Iannotta D, Kijas AA, Rowan AW, Wolfram AE. Entry and exit of extracellular vesicles to and from the blood circulation. Nat Nanotechnol. 2024;19:13–20.
39. Modasia AA, Jones EJ, Martel LM, Louvel H, Couraud PO, Blackshaw LA, Carding SR. The use of a multicellular in vitro model to investigate uptake and migration of bacterial extracellular vesicles derived from the human gut commensal Bacteroides thetaiotaomicron. J Extracell Biol. 2023;2:e93.
40. van Niel G, D'Angelo G, Raposo G. Shedding light on the cell biology of extracellular vesicles. Nat Rev Mol Cell Biol. 2018;19:213–28.
41. De Rose V, Molloy K, Gohy S, Pilette C, Greene CM. Airway epithelium dysfunction in cystic fibrosis and COPD. Mediators Inflamm. 2018;2018:1309746.
42. Petrache I, Pujadas E, Ganju A, Serban KA, Borowiec A, Babbs B, Bronova IA, Egersdorf N, Hume PS, Goel K et al. Marked elevations in lung and plasma ceramide in COVID-19 linked to microvascular injury. JCI Insight. 2023;8.

43. Hartmann D, Lucks J, Fuchs S, Schiffmann S, Schreiber Y, Ferreiros N, Merkens J, Marschalek R, Geisslinger G, Grosch S. Long chain ceramides and very long chain ceramides have opposite effects on human breast and colon cancer cell growth. Int J Biochem Cell Biol. 2012;44:620–8.
44. Bazzan E, Radu CM, Tine M, Neri T, Biondini D, Semenzato U, Casara A, Balestro E, Simioni P, Celi A, et al. Microvesicles in Bronchoalveolar lavage as a potential biomarker of COPD. Am J Physiol Lung Cell Mol Physiol. 2021;320:L241–5.
45. Haque S, Kodidela S, Sinha N, Kumar P, Cory TJ, Kumar S. Differential packaging of inflammatory cytokines/ chemokines and oxidative stress modulators in U937 and U1 macrophages-derived extracellular vesicles upon exposure to tobacco constituents. PLoS ONE. 2020;15:e0233054.
46. Qin J, Kilkus J, Dawson G. The hyaluronic acid inhibitor 4-methylumbelliferone is an NSMase2 activator-role of ceramide in MU anti-tumor activity. Biochim Biophys Acta. 2016;1861:78–90.
47. Oaks J, Ogretmen B. Regulation of PP2A by sphingolipid metabolism and signaling. Front Oncol. 2014;4:388.
48. Squecco R, Pierucci F, Idrizaj E, Frati A, Lenci E, Vicenti C, Iachini MC, Martinesi M, Garella R, Baccari MC, et al. Ceramide/protein phosphatase 2A axis is engaged in gap junction impairment elicited by PCB153 in liver stem-like progenitor cells. Mol Cell Biochem. 2021;476:3111–26.
49. Okamoto T, Usuda H, Tanaka T, Wada K, Shimaoka M. The functional implications of endothelial gap junctions and cellular mechanics in vascular angiogenesis. Cancers (Basel). 2019;11.
50. Pohl U, Connexins. Key players in the control of vascular plasticity and function. Physiol Rev. 2020;100:525–72.
51. Veliz LP, Gonzalez FG, Duling BR, Saez JC, Boric MP. Functional role of gap junctions in cytokine-induced leukocyte adhesion to endothelium in vivo. Am J Physiol Heart Circ Physiol. 2008;295:H1056–66.
52. Vliagoftis H, Ebeling C, Ilarraza R, Mahmudi-Azer S, Abel M, Adamko D, Befus AD, Moqbel R. Connexin 43 expression on peripheral blood eosinophils: role of gap junctions in transendothelial migration. Biomed Res Int. 2014;2014:803257.
53. Nagasawa K, Chiba H, Fujita H, Kojima T, Saito T, Endo T, Sawada N. Possible involvement of gap junctions in the barrier function of tight junctions of brain and lung endothelial cells. J Cell Physiol. 2006;208:123–32.
54. Mannell H, Kameritsch P, Beck H, Pfeifer A, Pohl U, Pogoda K. Cx43 promotes endothelial cell migration and angiogenesis via the tyrosine phosphatase SHP-2. Int J Mol Sci. 2021;23.
55. Kameritsch P, Kiemer F, Beck H, Pohl U, Pogoda K. Cx43 increases serum induced filopodia formation via activation of p21-activated protein kinase 1. Biochim Biophys Acta. 2015;1853:2907–17.
56. Wang DG, Zhang FX, Chen ML, Zhu HJ, Yang B, Cao KJ. Cx43 in mesenchymal stem cells promotes angiogenesis of the infarcted heart independent of gap junctions. Mol Med Rep. 2014;9:1095–102.
57. York AG, Skadow MH, Oh J, Qu R, Zhou QD, Hsieh WY, Mowel WK, Brewer JR, Kaffe E, Williams KJ, et al. IL-10 constrains sphingolipid metabolism to limit inflammation. Nature. 2024;627:628–35.
58. Lapperre TS, Postma DS, Gosman MM, Snoeck-Stroband JB, ten Hacken NH, Hiemstra PS, Timens W, Sterk PJ, Mauad T. Relation between duration of smoking cessation and bronchial inflammation in COPD. Thorax. 2006;61:115–21.
59. Catalano M, O'Driscoll L. Inhibiting extracellular vesicles formation and release: a review of EV inhibitors. J Extracell Vesicles. 2020;9:1703244.
60. Amersfoort J, Eelen G, Carmeliet P. Immunomodulation by endothelial cells - partnering up with the immune system? Nat Rev Immunol. 2022;22:576–88.

Publisher's note